



저작자표시-비영리-변경금지 2.0 대한민국

이용자는 아래의 조건을 따르는 경우에 한하여 자유롭게

- 이 저작물을 복제, 배포, 전송, 전시, 공연 및 방송할 수 있습니다.

다음과 같은 조건을 따라야 합니다:



저작자표시. 귀하는 원저작자를 표시하여야 합니다.



비영리. 귀하는 이 저작물을 영리 목적으로 이용할 수 없습니다.



변경금지. 귀하는 이 저작물을 개작, 변형 또는 가공할 수 없습니다.

- 귀하는, 이 저작물의 재이용이나 배포의 경우, 이 저작물에 적용된 이용허락조건을 명확하게 나타내어야 합니다.
- 저작권자로부터 별도의 허가를 받으면 이러한 조건들은 적용되지 않습니다.

저작권법에 따른 이용자의 권리는 위의 내용에 의하여 영향을 받지 않습니다.

이것은 [이용허락규약\(Legal Code\)](#)을 이해하기 쉽게 요약한 것입니다.

[Disclaimer](#)

공학박사 학위논문

**Brownian dynamics simulation on  
the heterogeneous structure formation  
in the drying of colloidal films**

브라운 동력학 전산모사를 이용한 입자계 필름의 건조  
과정에서의 불균일 구조 형성과정 연구

2022 년 2 월

서울대학교 대학원

화학생물공학부

정 재 환

**Brownian dynamics simulation on  
the heterogeneous structure formation  
in the drying of colloidal films**

브라운 동력학 전산모사를 이용한 입자계 필름의 건조  
과정에서의 불균일 구조 형성과정 연구

지도 교수 안 경 현

이 논문을 공학박사 학위논문으로 제출함  
2022년 2월

서울대학교 대학원  
화학생물공학부  
정 재 환

정재환의 공학박사 학위논문을 인준함  
2022년 2월

위 원 장 \_\_\_\_\_ (인)

부위원장 \_\_\_\_\_ (인)

위 원 \_\_\_\_\_ (인)

위 원 \_\_\_\_\_ (인)

위 원 \_\_\_\_\_ (인)

## **Abstract**

# **Brownian dynamics simulation on the heterogeneous structure formation in the drying of colloidal films**

Jae Hwan Jeong

School of Chemical and Biological Engineering

The Graduate School

Seoul National University

Colloidal films are composed of complex mixtures of particles with different sizes, binders, solvents, and additives. The control of their particle size distribution is a critical part of applications. Although the colloidal system is well-dispersed before drying, colloidal films could exhibit structural heterogeneity during the drying process. Several studies have been performed to figure out the heterogeneity in drying films, however, they were mainly focused on the drying conditions where the heterogeneity was observed. In this thesis, stress and microstructural developments during the drying process were investigated to understand the formation mechanism of heterogeneous

structure. As a model system for complex colloidal films, mono- and bi-disperse colloidal films were studied by using the numerical approach.

First, in the monodisperse colloidal films, the formation of vertical structural heterogeneity was examined by using the Brownian dynamics simulation. The time scale ratio between the evaporation rate and the particle diffusion rate was the key factor in inducing structural heterogeneity. When the evaporation rate was dominant, the particles were accumulated near the evaporating interface, causing the accumulation region to grow. Accumulated particles contributed to the localization of the normal stress, inducing a continuous increase of the normal stress at the interface. The normal stress difference formed across the film was found to be the driving force of the net motion of the particles. The normal stress difference was also correlated with microstructural development, which provided a full understanding of the heterogeneity formation mechanism.

Second, in the bi-disperse colloidal films, the formation of a stratified layer consisting of only small particles was studied by using the Brownian dynamics simulation. When the evaporation rate was more dominant than the particle diffusion rate, the small particles were accumulated near the interface, forming the stratified layer. The large particles were depleted near the interface, forming an accumulation region below the stratified layer. These accumulated particles induced localization of the normal stress, so that the normal stress at the interface increased from the beginning of drying. The normal stress difference formed across the film was found to be the physical origin of

the force pushing the large particles away from the interface. Associating the microstructural development with the normal stress response, the force on the large particles was explained by the significant increase in the average number of small particles in contact with large ones.

The correlation between the normal stress and microstructural development provides systematic insight into the formation mechanism of heterogeneous structure in drying films. Thus the results of this thesis are expected to be beneficial in various technological fields to form the desired products through the drying process.

**Key words:** Drying, colloidal film, heterogeneity, stress, microstructure, particle diffusion, particle accumulation, stratification, Brownian dynamics simulation

**Student Number:** 2016–21054

# Contents

Abstract.....	i
List of Figures.....	vi
<b>Chapter 1. Introduction.....</b>	<b>1</b>
<b>Chapter 2. Drying mechanism of monodisperse colloidal film.....</b>	<b>6</b>
2.1. Introduction.....	7
2.2. Simulation methods.....	9
2.2.1. Model system.....	9
2.2.2. Brownian Dynamics (BD) simulation.....	12
2.2.3. Interaction potential.....	14
2.2.4. Normal stress calculation.....	16
2.3. Results and discussion.....	18
2.3.1 Particle distribution in drying film.....	18
2.3.2. Normal stress localization in drying film.....	26
2.3.3 Microstructural development.....	35
2.4. Summary.....	42
<b>Chapter 3 Drying mechanism of bi-disperse colloidal film.....</b>	<b>44</b>
3.1. Introduction.....	45
3.2. Simulation methods.....	48
3.2.1. Model system.....	48

3.2.2. Brownian Dynamics (BD) simulation.....	51
3.2.3. Interaction potential.....	52
3.2.4. Normal stress calculation.....	54
3.3. Results and discussion.....	55
3.3.1 Particle distribution in drying film.....	55
3.3.2. Normal stress localization in drying film.....	64
3.3.3 Microstructural development.....	75
3.4. Summary.....	87
<b>Chapter 4 Stratification mechanism on the local length scale.....</b>	<b>89</b>
4.1. Introduction.....	90
4.2. Derivation of the local force field.....	91
4.3. Results and discussion.....	95
4.3.1 Evolution of local force field.....	95
4.3.2. Local force field and local volume fraction profile.....	103
4.4. Summary.....	112
<b>Chapter 5 Concluding remark.....</b>	<b>113</b>
<b>References.....</b>	<b>119</b>
<b>국문초록.....</b>	<b>131</b>
<b>Curriculum Vitae.....</b>	<b>133</b>



## List of Figures

**Figure 2.1** Schematic diagram of the monodisperse colloidal film drying.  
 Left: side view, right: top view.....10

**Figure 2.2** Time evolution of particle configuration in drying film. (a)  $Pe = 6$ ; (b)  $Pe = 60$ .....19

**Figure 2.3** Local volume fraction profile with the film thickness during drying. (a)  $Pe = 6$ ; (b)  $Pe = 30$ ; (c)  $Pe = 60$ . The volume fraction in the model of Wang and Brady is the green dashed line, and the simulation the red solid line.  $H/H_0$  is denoted next to the corresponding profile. The blue dotted line indicates the  $z$ -coordinate included in the accumulation region where the local volume fraction is equal to  $\phi(z)=1.1\phi_0$  at  $H/H_0 = 0.8$  for all  $Pe$ .....21

**Figure 2.4** The position of the accumulation front with the film thickness. The blue dotted line and arrows indicate the thickness of the accumulation region at  $H/H_0 = 0.8$ .....25

**Figure 2.5** Local normal stress profile with the film thickness during drying. (a)  $Pe = 6$ ; (b)  $Pe = 30$ ; (c)  $Pe = 60$ . The black solid line represents the local normal stress profile at a given film thickness, and the pink solid line represents the normal stress at the interface over time (calculated by extrapolating to the position of the interface using the local normal stress value near the interface).....27

<b>Figure 2.6</b>	Development of local normal stress at the (a) interface ( $z = H$ ) and (b) substrate ( $z = a$ ).....	29
<b>Figure 2.7</b>	The scaled normal stress difference between the interface and substrate with the film thickness. The gray dotted line represents a guideline with a slope of $-1$ .....	31
<b>Figure 2.8</b>	Normalized average particle velocity in the $z$ -direction with the film thickness. A $(-)$ sign is used to convert the descending velocity in the $-z$ direction into a $(+)$ sign.....	32
<b>Figure 2.9</b>	Average contact number distribution of particles $P(z, N_c)$ at the interface and substrate with film thickness. (a) interface ( $z = H$ ); (b) substrate ( $z = a$ ). The blue dotted line represents the film thickness of the normal stress difference maximum (see Figure 2.7).....	36
<b>Figure 2.10</b>	2D planar pair-distribution function $g_{xy}(\mathbf{r}_{xy})$ (at $H/H_0 = 0.18$ ) at the interface ( $z = H$ ) and substrate ( $z = a$ ). Red lines represent $r_{xy} = 2a, 4a,$ and $6a$ from the left, respectively....	38
<b>Figure 3.1</b>	Schematic diagram of the bi-disperse colloidal film drying. The large particles are colored in red, and small in blue.....	50
<b>Figure 3.2</b>	Snapshots of the particle configuration in drying films. (a) $Pe_L = 6$ ; (b) $Pe_L = 60$ .....	56
<b>Figure 3.3</b>	Local volume fraction profile of the large and small particles during drying. The volume fraction from the substrate ( $z = a_L$ ) to the interface ( $z = H$ ) is shown at the corresponding film thickness.....	58

- Figure 3.4** Position  $z$  of accumulation front along the normalized film thickness ( $H/H_0$ ). The blue dotted line and arrows show the thickness of the accumulation region at  $H/H_0 = 0.8$ .....63
- Figure 3.5** Evolution of the local normal stress during drying. (a)  $Pe_L = 6$ ; (b)  $Pe_L = 30$ ; (c)  $Pe_L = 60$ . The local normal stress profile is shown in a black solid line, and the normal stress at the interface is shown in pink.  $H/H_0$  is denoted next to the corresponding local normal stress profile.....65
- Figure 3.6** Evolution of the scaled normal stress difference between the interface and substrate. The scaled normal stress difference observed in the monodisperse colloidal film is shown in a gray dotted line. The arrows indicate the maximum of each curve.....68
- Figure 3.7** Evolution of the normalized average velocity in the  $z$ -direction for each type of particle. The normalized average velocity in the monodisperse colloidal film is shown in a gray dotted line. The arrows indicate the maximum of each curve. A (-) sign is used to convert the descending velocity in the  $-z$  direction into a (+) sign.....71
- Figure 3.8** Evolution of the contact number distribution at the substrate  $P(z=a_L, N_C)$ . The contact number is computed for each type of contact: (a) large-large ( $N_{C,LL}$ ); (b) small-small ( $N_{C,SS}$ ); (c) large-small ( $N_{C,LS}$ ) contact.....76
- Figure 3.9** Evolution of the contact number distribution at the interface,  $P(H, N_C)$ , relative to the substrate,  $P(a_L, N_C)$ , i.e.,  $P(H, N_C) -$

$P(a, N_C)$ . (a) large–large ( $N_{C,LL}$ ); (b) small–small ( $N_{C,SS}$ ); (c) large–small ( $N_{C,LS}$ ) contact.....79

**Figure 3.10** 2D planar partial pair–distribution function for the position of the small particles based on the large particles,  $g_{xy}^{LS}(\mathbf{r}_{xy})$  (at  $H/H_0 = 0.18$ ), at the interface ( $z = H$ ) and substrate ( $z = a_L$ ). Red lines indicate the peaks near  $r_{xy} = a_L + a_s$ ,  $a_L + 3a_s$ , and  $3a_L + a_s$  from the left, respectively.....82

**Figure 3.11** 2D planar partial pair–distribution function for the position of the small particles based on the small particles,  $g_{xy}^{SS}(\mathbf{r}_{xy})$  (at  $H/H_0 = 0.18$ ), at the interface ( $z = H$ ) and substrate ( $z = a_L$ ). Red lines indicate the peaks near  $r_{xy} = 2a_s$ ,  $4a_s$ , and  $2a_L + 2a_s$  from the left, respectively.....84

**Figure 4.1** Evolution of the scaled local force field during drying at  $Pe_L = 60$ . The local force from the substrate ( $z = a_L$ ) to the interface ( $z = H$ ) is shown at the corresponding film thickness. The local force is computed according to the types of interacting particles. (a)  $f_z^{LL}(z)$ ; (b)  $f_z^{LS}(z)$ ; (c)  $f_z^{SS}(z)$ ; (d)  $f_z^{SL}(z)$ . A (–) sign is used to convert the force in the  $-z$  direction into a (+) sign.....96

**Figure 4.2** Zoom–in on the intercalated zone in the scaled local force field of small–large interaction,  $f_z^{SL}(z)$  for  $H/H_0 \leq 0.4$ . (b) Snapshot of the particle configuration near the substrate at  $H/H_0 = 0.18$  for  $Pe_L = 60$ .....99

**Figure 4.3** The evolution of the scaled local net force field during drying.

The local net force is the sum of the local forces according to the types of interaction.....100

**Figure 4.4** Scaled local force field near the interface at  $H/H_0 = 0.9$  for  $Pe_L = 60$ . (b) Local volume fraction profile near the interface at  $H/H_0 = 0.9$  for  $Pe_L = 60$ .....104

**Figure 4.5** Evolution of the scaled local force field of large–small interaction,  $f_z^{LS}(z)$ , and of the local volume fraction profile near the interface. The profile near the interface,  $(z-H)/H_0 \geq -0.20$ , is shown at the corresponding film thickness.....108

Chapter 1.

Introduction

Colloidal films are widely used in many applications, including latex painting,[1, 2] paper coating,[3] catalysts,[4] filters,[5] and battery electrodes.[6–8] In addition to chemical properties, structural properties, such as uniformity, microstructure, porosity, and film thickness, are of interest in these systems.[9, 10] Even colloidal films with the same formulation may show structural heterogeneity during the drying process.[11–13] For example, in the anode system of a Li-ion battery, the concentration of the binder is found to be higher at the air-solvent interface during drying.[14] In a mixture of charged and neutral particles, the volume fraction of the neutral particles is observed to be higher at the interface during drying.[15] Structural heterogeneity can be detrimental for the uniform product quality,[13] but can also be beneficial for multilayer coating in a single-step procedure.[16] Therefore, to form the desired final products, a full understanding is required of the drying process of colloidal films.

Mono- and bi-disperse colloidal films have been extensively studied as a model system for complex colloidal films. In the monodisperse colloidal films, several experimental studies have reported the vertical structural heterogeneity in drying films. Ma *et al.* visualized the structure development during the drying process of hard latex particles ( $\sim 0.5 \mu\text{m}$  radius).[17] In their research, the particles were accumulated at the descending air-water interface, forming a “consolidation front”. Similarly, Shimmin *et al.* observed that the particle volume fraction increases at the interface, resulting in the formation of colloidal crystals in the drying of hard latex particles ( $\sim 0.5 \mu\text{m}$  radius).[18] Cardinal *et al.*

further studied the distribution of silica particles in the drying film according to the particle size ( $0.1 \sim 0.5 \mu\text{m}$  radius), evaporation rate, and sedimentation rate.[19] Depending on the drying conditions, the particles were accumulated at the interface, or uniformly dispersed in the film, or deposited on the substrate.

In the bi-disperse colloidal films, some experimental studies reported a crystal structure formed in the drying process.[20–22] They observed various types of close-packed arrays, known as binary colloidal crystals (bCCs), by changing the size ratio and composition of the two types of particles (large and small particles). In addition to size and composition, systematic experimental studies have been conducted by varying the evaporation rate. In some of their studies, the volume fraction of the large particles was observed to be higher on the top surface of the final dried film (air–solvent interface in the drying film) (large–on–top).[2, 23–25] Also, the volume fraction of the large particles increased as the evaporation rate increased. Recently, however, Fortini *et al.* reported that a stratified layer consisting of only small particles was formed near the interface during the drying process.[26] They confirmed that this small–on–top stratification appeared at a high evaporation rate, size ratio, and volume fraction of the small particles. The small–on–top stratification has received a lot of attention for the multilayer coating application, and many experimental studies have been conducted to find the drying conditions where this phenomenon occurs.[22, 27]

Theoretical approaches have been developed to figure out the



structural heterogeneity in drying films.[28–32] In these studies, only the particle motion in the film thickness direction was considered, which assumed that the lateral flow is not important. They found that the particle distribution in the film thickness direction is affected by the evaporation rate and particle diffusion. The time scale of the evaporation rate,  $\tau_E = H_0 / \dot{E}$ , and the particle diffusion,  $\tau_D = H_0^2 / D$ , are quantified and related by the Peclet number,  $Pe = \tau_D / \tau_E = H_0 \dot{E} / D$ , where  $H_0$  is the initial film thickness,  $\dot{E}$  is the evaporation rate, and  $D$  is the particle diffusion coefficient. The change of volume fraction profile according to the Peclet number has been studied and verified in several experimental and modeling studies.[19, 24, 33, 34] When  $Pe > 1$ , the evaporation rate dominates, and the particles are accumulated at the descending interface. On the other hand, when  $Pe < 1$ , the particles are distributed uniformly throughout the film due to the diffusion of the particles.

Although continuum models were proven useful in predicting the particle accumulation in drying films, there were limitations in explaining various heterogeneous structures that experimental studies observed. In addition, the models could not capture the evolution of stress and microstructure during the drying process. Therefore, the necessity of simulation studies has been emphasized to understand the mechanism of the drying process.[35] In this thesis, inspired by the limitations of previous works, we focus on the investigation of the detailed drying mechanism of colloidal films. For this purpose, we employ the Brownian dynamics simulation to describe the drying of mono- and bi-disperse colloidal films.

This thesis is organized as follows. In Chapter 2, the drying mechanism of the monodisperse colloidal films is analyzed in three aspects: accumulation front, normal stress, and microstructure. In Chapter 3, the drying mechanism of the bi-disperse colloidal films is investigated. The evolution of normal stress is analyzed according to the occurrence of small-on-top stratification and related to microstructural development. In Chapter 4, the stratification mechanism is investigated on the local length scale. The local force acting on each type of particle is derived by decomposing the local normal stress to explain the physical origin of the stratification. The thesis is concluded in Chapter 5 with a summary.

## Chapter 2.

### Drying mechanism of monodisperse colloidal film

## 2.1 Introduction

Several simulation studies have been conducted to figure out the drying mechanism of monodisperse colloidal film. Reyes and Duda described the drying process of monodisperse colloidal films using the Monte Carlo simulation method.[36] The volume fraction profile was observed in the film thickness direction during drying, and particle arrangement was investigated in the final dried film. Cheng and Grest showed the influence of the evaporation rate on the particle distribution and arrangement using the molecular dynamics simulation method.[37] Most of the previous simulation studies mainly focused on the change in particle distribution according to the drying conditions.[36–39]

There have been few simulation studies on the drying mechanism in terms of the evolution of stress and microstructure. Recently, Wang and Brady observed the evolution of the normal stress and the microstructure at the final stage using the Brownian dynamics simulation.[40] As a result, a master curve of the normal stress was found at high Peclet number, and they explained it in terms of the convective transport in the film. However, there was a limited explanation of the correlation between the normal stress and microstructural development. Howard *et al.* intensively studied the crystallization kinetics in drying film using the molecular dynamics simulation method, but the normal stress was not investigated.[41]

In this chapter, we focus on the investigation of the detailed drying mechanism of monodisperse hard–sphere colloidal film. For this purpose, simulations are conducted by using the Brownian dynamics simulation

over a wide range of Peclet numbers. Firstly, the evolution of the particle distribution is carefully investigated. The particle distribution is quantitatively analyzed by defining an accumulation front and observing its growth during drying. Furthermore, the evolution of the normal stress is also quantitatively analyzed in terms of a scaled normal stress difference across the film. In addition, by performing a more detailed analysis of the microstructural development, we examine the direct correlation of the particle distribution, normal stress, and microstructure in the drying film.

## 2.2 Simulation methods

### 2.2.1 Model system

The model system is as follows. Hard-sphere colloidal particles with  $0.5 \mu\text{m}$  radius are dispersed in a Newtonian fluid (initial volume fraction  $\phi_0 = 0.1$ ). The initial film thickness is  $30 \mu\text{m}$ , and the evaporation rate is fixed ranging from  $5 - 50 \mu\text{m}/\text{min}$  (i.e. the decrease rate of the interface position). This model well describes the actual film drying process of monodisperse silica particles with the evaporation rate (approximately  $2 - 80 \mu\text{m}/\text{min}$ ) in air.[19]

The assumptions of the drying simulation are based on that of the drying models of monodisperse colloidal films.[29, 40] In their models, the solvent was evaporated from a thin film, assuming that the motion in the lateral direction was not important. Also, the evaporation rate was constant during drying, so that the film thickness decreased at a constant rate. In addition, there was no bulk flow in the film, and the distribution of the particles changed by the descending interface and the particle diffusion.

These conditions are re-established to the three-dimensional (3D) system under the simulation platform (see Figure 2.1). The colloidal film is covered on a stationary planar substrate ( $z = 0$ ). The neutrally buoyant hard-sphere particles with radius  $a$  are randomly distributed in the film with an initial particle volume fraction  $\phi_0 = 0.1$  (the number of particles  $N = 2,000$ ). In the  $x$ - and  $y$ -directions, we set the domain size to  $40a$  with periodic boundary conditions. To impose periodic boundary

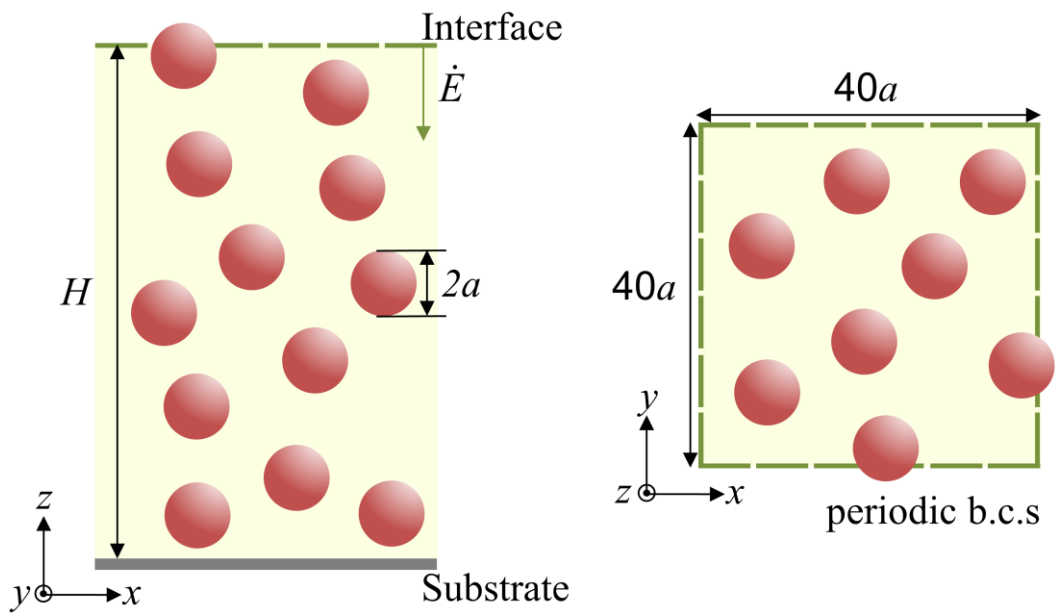


**Figure 2.1** Schematic diagram of the monodisperse colloidal film drying. Left: side view, right: top view.

conditions, four sides of the simulation box in the  $x$ - and  $y$ -directions are surrounded by an infinite set of replicas. The initial film thickness is  $H_0 = 60a$ , and the interface descends in the  $z$ -direction at a constant evaporation rate during the drying process. The drying is continued until a final film thickness of  $H = 0.18 H_0$  is reached, where the bulk volume fraction of the film becomes  $\phi_{\text{bulk}} = 0.55$ . The simulations are conducted with the evaporation rates  $\dot{E} = 6, 30, \text{ and } 60 H_0/\tau_D$ , which correspond to Peclet number  $Pe (= \tau_D/\tau_E = H_0\dot{E}/D) = 6, 30, \text{ and } 60$ , respectively ( $D = k_B T/\zeta$  from the Einstein–Stokes relation, with  $k_B$  the Boltzmann constant,  $T$  the temperature,  $\zeta$  the single–particle friction coefficient). Simulations are conducted with ten different initial configurations for each  $Pe$ .

In the drying process of monodisperse colloidal films, the evaporation rate is initially constant, which is the constant rate period (CRP),” and then decreases, called the “falling rate period (FRP).” [30, 42] In general, the FRP begins when the bulk volume fraction of the film is higher than 0.6. In this study, drying is continued until the bulk volume fraction becomes 0.55 so that the constant evaporation rate is a reasonable assumption in this study.



### 2.2.2 Brownian Dynamics (BD) simulation

Brownian dynamics simulation (BD) is introduced to study the colloidal film drying process.[43, 44] The motion of the particle is described by the overdamped Langevin equation

$$\mathbf{0} = -\zeta \dot{\mathbf{r}}_i + \mathbf{f}_i^P + \mathbf{f}_i^S + \mathbf{f}_i^I + \mathbf{f}_i^B. \quad (2.1)$$

The first term on the right-hand side of eqn (2.1) is the hydrodynamic force acting on the particle (Stokes friction  $\zeta=6\pi\eta a$ , with  $\eta$  the solvent viscosity).  $\mathbf{f}_i^P$  is the force due to the interaction between particles,  $\mathbf{f}_i^S$  is the force from the substrate, and  $\mathbf{f}_i^I$  represents the capillary force at the (air-solvent) interface. As a result of the continuous evaporation of the solvent, the interface descends at a constant velocity and pushes the particles with the force of  $\mathbf{f}_i^I$ . Here,  $\mathbf{f}_i^P = -\sum_j \partial U_{ij}^P / \partial \mathbf{x}_i$  from the potential ( $U_{ij}^P$ ) between the particles  $i$  and  $j$ , where  $\mathbf{f}_i^S = -\partial U_i^S / \partial \mathbf{x}_i$  and  $\mathbf{f}_i^I = -\partial U_i^I / \partial \mathbf{x}_i$  from the particle-wall potential ( $U_i^S$ ) and particle-interface potential ( $U_i^I$ ), respectively. These three forces are obtained by differentiating the potentials. The Brownian force  $\mathbf{f}_i^B$  is generated as a random number with zero mean and variance  $\langle \mathbf{f}_i^B(t) \mathbf{f}_i^B(t') \rangle = 2\zeta k_B T \delta(t-t') \mathbf{I}$ . The aforementioned Langevin equation is numerically solved by the Euler method.[45] The (dimensionless) time step is set as  $\Delta t = 10^{-8} H_0^2 / D$ , which is small enough to prevent the overlap of the particles.

In the BD simulation, the solvent is treated as an implicit viscous

background, such that hydrodynamic interactions (HI), the flow passing the particles, and the capillary force are neglected. Recently, Tang *et al.* described the drying process of bi-disperse colloidal films using both the explicit and implicit solvent methods to investigate the effect of HI and the flow passing the particles.[46] They observed the volume fraction profile in the  $z$ -direction during the drying process until  $H/H_0 = 0.25$  (initial volume fraction = 0.1) and found that the results were almost identical in the two methods. In addition, Fujita and Yamaguchi described the drying of colloidal films in consideration of the capillary force acting on the particles at the interface.[47] They found that structural defects were caused by the increasing effect of the capillary force as drying progressed. However, the defects were observed for the particle volume fraction higher than 0.7. These observations indicate that the BD simulation can effectively describe the drying process of colloidal films despite the implicit solvent method.

### 2.2.3 Interaction potential

The interaction of the (nearly) hard-sphere particles is modeled using the Weeks-Chandler-Andersen (WCA) type potential with the exponents of (96-48) where an increase in the exponents changes the steepness of the potential approaching the hard-sphere potential.[48-50] We have chosen exponents such that the normal stress evaluated in the simulation is comparable to the stress in the potential-free algorithm, designed to perform BD simulations on model hard spheres.[40] The potential between the particles  $i$  and  $j$  is given in the form

$$U_{ij}^P(r_{ij}) = \begin{cases} 4\varepsilon \left[ \left( \frac{\sigma}{r_{ij}} \right)^{96} - \left( \frac{\sigma}{r_{ij}} \right)^{48} + \frac{1}{4} \right] & r_{ij} < 2^{1/48} \sigma \\ 0 & r_{ij} > 2^{1/48} \sigma \end{cases} \quad (2.2)$$

where  $r_{ij}$  is the distance between the centers of the particles,  $\sigma = 2a$  is the effective diameter,  $\varepsilon$  is the parameter that determines the strength of the repulsion and we set  $\varepsilon = 1k_B T$ .

The interaction between the particle and substrate is also described by the WCA potential (96-48) [51, 52]

$$U_i^S(z_i) = \begin{cases} 4\varepsilon \left[ \left( \frac{\sigma}{z_i + a} \right)^{96} - \left( \frac{\sigma}{z_i + a} \right)^{48} + \frac{1}{4} \right] & z_i + a < 2^{1/48} \sigma \\ 0 & z_i + a > 2^{1/48} \sigma \end{cases}. \quad (2.3)$$

Eqn (2.3) indicates that the repulsive force is applied on a particle by a virtual wall particle at a distance  $a$  from the substrate ( $z = 0$ ) in the  $-z$  direction.[51, 52] Here,  $z_i$  is the height of the particle's center above the

substrate.

We model the soft film interface by the purely repulsive harmonic potential.[26, 49] This potential assumes a contact angle of  $90^\circ$  between a particle and the interface so that only the vertical capillary force is considered, neglecting the lateral capillary force.[53, 54] Thus, drying simulations can be performed under conditions similar to existing studies that do not take into account the lateral flow. The expression is given as

$$U_i^I(z_i) = \begin{cases} 0 & z_i < H \\ \kappa(z_i - H)^2/2 & H \leq z_i < H^c \\ \kappa(H^c - H)^2/2 - F^g(z_i - H^c) & z_i \geq H^c \end{cases} \quad (2.4)$$

where  $\kappa$  is a spring constant that reflects the surface tension between a particle and the interface. We take  $\kappa = 1000\epsilon/a^2$ , which is large enough to move the particles along with the interface and small enough to be numerically stable.[49, 55]  $H^c = H + a$  is a cutoff height, where a particle completely escapes from the film and descends due to gravity  $F^g$ . The term  $F^g = -\kappa(H^c - H)$  is defined to ensure that the force exerted on the particle is continuous at  $z = H^c$ . In short, when the center of the particle is within  $H \leq z_i < H^c$ , the particle moves down by the force proportional to the distance from the interface, and it descends only by  $F^g$  when the particle completely leaves the film ( $z_i \geq H^c$ ).

## 2.2.4 Normal stress calculation

We calculate the local normal stress in the  $z$ -direction. The  $zz$  component of the local normal stress,  $\Sigma_{zz}(z)$ , is expressed by the method of planes (MOP) [56, 57]

$$\langle \Sigma_{zz}(z) \rangle = -\langle n(z) \rangle k_B T - \frac{1}{2A} \left\langle \sum_{i=1}^N f_{iz}^P \operatorname{sgn}(z_i - z) \right\rangle \quad (2.5)$$

where  $\langle \cdot \rangle$  represents an ensemble average,  $n(z)$  is the local number density of the particles, and  $A$  is the cross-sectional ( $x$ - $y$  plane) area of the simulation box.  $f_{iz}^P$  is the  $z$  component of the total inter-particle forces acting on the particle  $i$ .  $\operatorname{sgn}(\cdot)$  is a sign operator, which returns 1 or  $-1$  when the input value is positive or negative, respectively. The first term on the right-hand side in eqn (2.5),  $-\langle n(z) \rangle k_B T$ , is the normal stress associated with the thermal energy of the Brownian particles. And the second term,  $-\frac{1}{2A} \left\langle \sum_{i=1}^N f_{iz}^P \operatorname{sgn}(z_i - z) \right\rangle$ , is the inter-particle stress, which originates from the inter-particle forces.

The normal stress calculated from the previous equation includes only the contributions of the inter-particle forces where the forces from the substrate and interface are not considered. In addition, the MOP considers all particle pairs interacting across each plane to calculate the stress. Accordingly, the stress is calculated from a larger number of samples in the MOP compared to the spatial binning method, which helps to reduce stress noise (statistical error). [56]

Note that the hydrodynamic interactions (HI) are not captured in this

study. Recently, Chu and Zia analyzed the normal stress by controlling the range of HI and Peclet number ( $Pe$ ). [58] When considering long-range HI alone, the dependence of normal stress on the Peclet number was scaled to  $\sim Pe$ , in agreement with the results of non-hydrodynamically interacting colloids. [59] When considering the short-range HI, HI acted to suppress the normal stress development, and the dependence of the normal stress on the Peclet number changed to  $\sim Pe^{0.8}$ . In the drying process, the volume fraction of the film increases as drying progresses, inducing an increase in the contact between the particles. Thus the long-range HI is important at the initial stage of drying and the short-range HI becomes stronger as drying proceeds. This implies that the calculated normal stress in our study accurately captures the drying mechanism at the initial stage though hydrodynamic interaction is absent. On the other hand, the calculated normal stress can miss the effect of HI in the later stage of drying. But, this missing point is not significant based on the normal stress scaling in the range of Peclet number  $Pe = 6 - 60$  we cover. Therefore, our results capture some important features of the drying mechanism during the overall drying process.

## 2.3 Results and discussion

### 2.3.1 Particle distribution in drying film

Figure 2.2 shows the simulation snapshots of particle configurations at different Peclet number ( $Pe$ ). In this figure, the film thickness ( $H$ ) is normalized to the initial film thickness ( $H_0$ ), so it decreases from 1.0 with time. Drying simulations are conducted for  $5800000\Delta t$  for the final stage at  $Pe = 6$ , which is ten times larger than that at  $Pe = 60$ .

When  $Pe = 6$  (Figure 2.2(a)), the particles are more concentrated near the interface than in the bulk at  $H/H_0 = 0.8$ . This can be understood that the interface descends faster than the particle diffusion, leading to an accumulation of particles at the interface. And a dense particle distribution is also observed near the substrate in  $H/H_0 \leq 0.6$ . When  $Pe = 60$  (Figure 2.2(b)), the evaporation is more dominant and the concentrated layer of particles is formed near the interface even until  $H/H_0 = 0.4$ . However, the particle distribution near the substrate does not change when  $H/H_0 \geq 0.4$  and becomes denser between  $H/H_0 = 0.4$  and 0.3.

These simulation results are similar to the experimental results of a colloidal film drying for  $Pe \approx 4$  and 200, respectively.[19] Cardinal *et al.* observed the cross-section of the drying film at different film thicknesses using cryo-SEM.[19] They found that the distribution of silica particles was almost uniform in the entire film at  $H/H_0 = 0.6$  for  $Pe \approx 4$ . For  $Pe \approx 200$ , however, the particles were initially accumulated at the interface to form an ordered structure, and the accumulation region

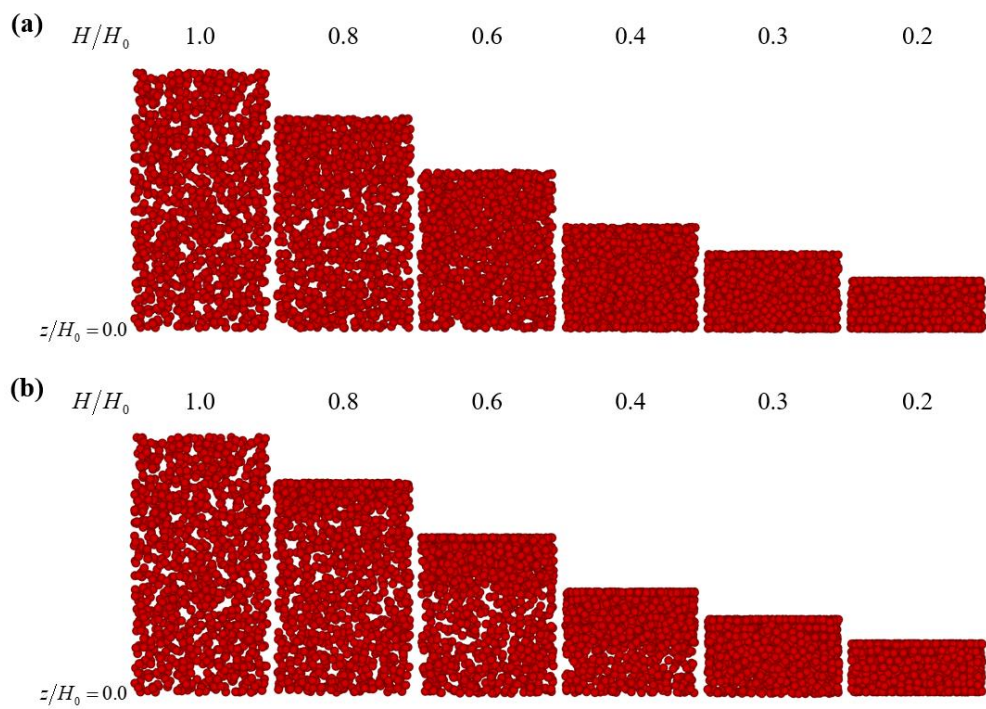


**Figure 1.2** Time evolution of particle configuration in drying film. (a)  $Pe = 6$ ; (b)  $Pe = 60$ .



grew from the interface as the drying proceeded.

Next, the changes in the particle distribution are quantitatively examined. Figure 2.3 shows the local volume fraction profile with the film thickness  $H/H_0$  over the  $z$ -axis ( $z/H_0$ ) of bin width  $0.02a$ . All simulation results are averaged over ten different initial configurations.

We verified our simulation results according to the drying model from Wang and Brady at different  $Pe$  prior to carrying out a full-scale analysis.[40] This model is based on the conservation equation of hard-sphere fluids expressed by a semi-empirical compressibility factor.[60] The particle distribution in the drying film was predicted by considering the collective diffusion coefficient according to the particle volume fraction.[40] When comparing the simulation results with the model prediction (Figure 2.3), the oscillation is observed in the volume fraction profile and its amplitude increases as the film thickness decreases. This oscillation is attributed to the packing of particles by the boundary.[61] In the drying process, the colloidal film is confined between the two boundaries and the volume fraction increases as the drying continues, which induces the packing of particles and intensifies the oscillation with time.[62] Furthermore, the volume fraction profile is almost identical in the two methods except near the two boundaries, at all  $Pe$  ( $Pe = 6 - 60$ ) explored in the study. This means that the simulation describes the drying mechanics of the hard-sphere colloidal film well. However, at the two boundaries in the simulation, the particles can exist above the interface and cannot approach the substrate closer than the particle radius. In contrast, the boundary effects are not considered in the

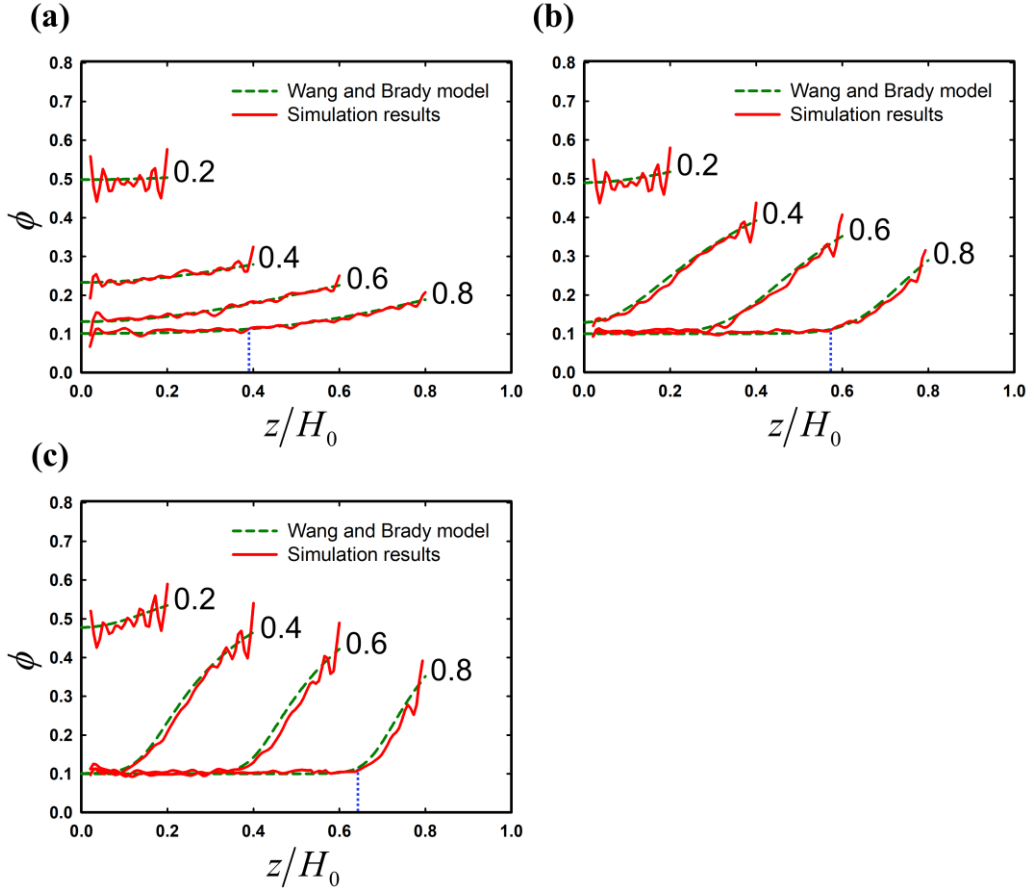


**Figure 2.2** Local volume fraction profile with the film thickness during drying. (a)  $Pe = 6$ ; (b)  $Pe = 30$ ; (c)  $Pe = 60$ . The volume fraction in the model of Wang and Brady is the green dashed line, and the simulation the red solid line.  $H/H_0$  is denoted next to the corresponding profile. The blue dotted line indicates the  $z$ -coordinate included in the accumulation region where the local volume fraction is equal to  $\phi(z) = 1.1\phi_0$  at  $H/H_0 = 0.8$  for all  $Pe$ .

modeling, which induces a discrepancy between the two approaches.

The local volume fraction profile at  $Pe = 6$  is plotted in Figure 2.3(a). At  $H/H_0 = 0.8$ , the volume fraction at the interface ( $z/H_0 = 0.8$ ) is about 0.2 and is higher than that at the substrate. Clearly, some particles are accumulated at the descending interface. These accumulated particles diffuse in the direction of the substrate to resolve the volume fraction gradient and form an “accumulation region.” [34, 49, 63] In this study, we judge the position ( $z$ ) in the film that is included in the accumulation region if the volume fraction is more than 10% higher than the initial volume fraction (i.e.,  $\phi(z) > 1.1\phi_0$ ). Below this accumulation region, there is a region that is not affected by the descending interface and maintains an initial volume fraction of 0.1, which appears in  $z/H_0 < 0.4$  at  $H/H_0 = 0.8$ , for example. The accumulation region grown from the interface reaches the substrate at  $H/H_0 > 0.6$ . In turn, the volume fraction at the substrate starts to increase. As the drying process continues, the volume fraction increases in the entire film, and its gradient formed in the vertical direction gradually decreases. At  $H/H_0 = 0.2$ , close to the final drying stage, the volume fraction profile becomes almost uniform across the film.

When  $Pe = 30$  in Figure 2.3(b), at  $H/H_0 = 0.8$ , the volume fraction at the interface is 0.3, which is slightly higher than when compared to the same film thickness of  $Pe = 6$ . The accumulation region is formed in  $0.6 < z/H_0 \leq 0.8$  where a volume fraction gradient is developed. At  $H/H_0 = 0.6$ , the thickness of the accumulation region is about  $0.31H_0$ , which is increased by  $0.08H_0$  when compared to the  $0.23H_0$  at  $H/H_0 = 0.8$ . In

contrast to the increasing volume fraction at the interface, the volume fraction near the substrate shows a modest change in  $H/H_0 \geq 0.6$ . Near the substrate, the volume fraction still maintains its initial volume fraction of 0.1 even after  $H/H_0 = 0.6$ , and then rapidly increases from  $H/H_0 \sim 0.4$  as the accumulation region reaches the substrate. Finally, the volume fraction is comparable to that at the interface for  $H/H_0 = 0.2$ . When  $Pe = 60$  (Figure 2.3(c)), we can confirm that the accumulation of particles is accelerated by faster evaporation. Compared to  $Pe = 6$  and 30, the volume fraction is higher at the interface at the same film thickness, whereas the thickness of the accumulation region is lower ( $0.16H_0$  at  $H/H_0 = 0.8$ ). In addition, the volume fraction near the substrate starts to increase at the lower film thickness ( $H/H_0 < 0.4$ ).

To quantify the development of the accumulation region in the drying film, the position  $z$  of the accumulation front is tracked according to the film thickness. We define the minimum value of the  $z$ -coordinates included in the accumulation region as the position of the accumulation front. In Figure 2.4, the evolution of the accumulation front is shown with the position of the interface (Note that the accumulation front at the initial stage in  $H/H_0 > 0.96$  is not shown, because it is difficult to precisely locate the accumulation front). When comparing at the same film thickness, the gap between the interface and the accumulation front is larger at lower  $Pe$ . For example, at  $H/H_0 = 0.8$ , this distance is  $0.41H_0$  for  $Pe = 6$ ,  $0.22H_0$  for  $Pe = 30$ , and  $0.16H_0$  for  $Pe = 60$ . This result can be explained that at lower  $Pe$ , it takes longer time to be dried to a specific film thickness under the same initial film thickness condition so

that the particles in the accumulation region can diffuse further from the interface. Moreover, at all  $Pe$ , the accumulation front descends faster than the interface and the thickness of the accumulation region increases over time. When observing at the substrate, the accumulation front reaches the substrate much earlier at lower  $Pe$ . The film thickness where the accumulation front contacts the substrate is  $H/H_0 = 0.64$  for  $Pe = 6$ ,  $H/H_0 = 0.44$  for  $Pe = 30$ , and  $H/H_0 = 0.33$  for  $Pe = 60$ , respectively.

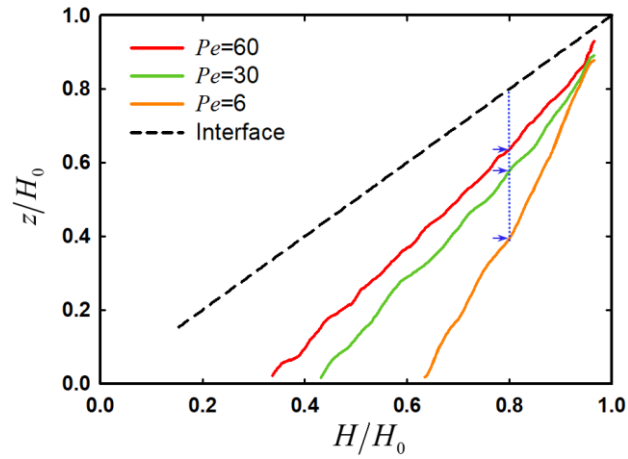


**Figure 2.3** The position of the accumulation front with the film thickness. The blue dotted line and arrows indicate the thickness of the accumulation region at  $H/H_0 = 0.8$ .

### 2.3.2 Normal stress localization in drying film

The local normal stress profile in the drying film is shown in Figure 2.5. The local normal stress calculated by eqn (2.5) is non-dimensionalized by  $k_B T / a^3$ . Note that at the initial stage,  $H/H_0 > 0.96$ , a large noise is generated during normal stress calculation due to insufficient particle number density at the interface. For this reason, it is not shown in the plot.

The local normal stress profile (Figure 2.5) has an almost identical pattern to the local volume fraction profile (Figure 2.3) for all  $Pe$ . This suggests that the particle volume fraction significantly contributes to the normal stress distribution. At low  $Pe$  (Figure 2.5(a)), the normal stress difference in the  $z$ -direction is small, indicating that the normal stress perturbation caused by the moving interface is stabilized by particle diffusion. Consequently, the normal stress becomes uniform throughout the film. At higher  $Pe$ , the evaporation becomes more dominant than particle diffusion, i.e. limited time to stabilize the perturbation of normal stress, so that the normal stress difference between the interface and the substrate gradually increases over time (Figures 2.5(b) and (c)). [64–66] Moreover, at the same film thickness, the normal stress at the interface for  $Pe = 60$  (Figure 2.5(c)) is higher than that for  $Pe = 30$  (Figure 2.5(b)), which can be attributed to the increased particle accumulation at the interface. When  $Pe = 6$  near the substrate, the normal stress shows no change until  $H/H_0 \sim 0.6$ , before increasing thereafter. At higher  $Pe$ , the normal stress remains at the initial value until  $H/H_0 \sim 0.4$  for  $Pe = 30$  and  $H/H_0 \sim 0.3$  for  $Pe = 60$ , which is followed

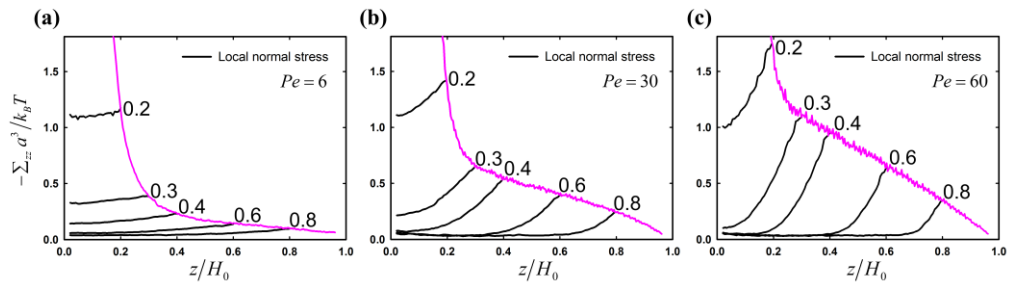


**Figure 2.4** Local normal stress profile with the film thickness during drying. (a)  $Pe = 6$ ; (b)  $Pe = 30$ ; (c)  $Pe = 60$ . The black solid line represents the local normal stress profile at a given film thickness, and the pink solid line represents the normal stress at the interface over time (calculated by extrapolating to the position of the interface using the local normal stress value near the interface).



by a drastic increase over time.

We thoroughly examine the localization of normal stress during drying. To this end, the time evolution of the normal stress is observed at the interface ( $z = H$ ) and the substrate ( $z = a$ ). In Figure 2.6(a), the normal stress at the interface increases from the beginning of drying regardless of  $Pe$ . This increase is induced by the accumulation of particles at the interface due to the strong evaporation. On the other hand, a different stress evolution is observed at the substrate (Figure 2.6(b)). In the  $Pe$  range of this study, the normal stress at the substrate is consistent with the low initial value even when the film is dried considerably (i.e.,  $H/H_0 = 0.7$ ). The film thickness where the normal stress begins to increase is different for  $Pe$ , such that  $H/H_0 = 0.63$  for  $Pe = 6$ ,  $H/H_0 = 0.42$  for  $Pe = 30$ , and  $H/H_0 = 0.33$  for  $Pe = 60$ . In other words, the increase of normal stress begins at higher film thickness (early stage of drying) for lower evaporation rate. Interestingly, it is confirmed that the film thickness of the initial stress increase is very similar to the film thickness where the accumulation front starts to touch the substrate (see Figure 2.4). These results directly prove that the normal stress evolution is further accelerated as the accumulation front reaches the substrate.

Assuming a one-dimensional system where only the drying in the vertical direction ( $z$ -direction) is relevant, the gradient in the  $zz$ -component of the normal stress is equal to the force in  $z$ -direction applied to the unit volume of the particle. This is the microscopic expression [67, 68]

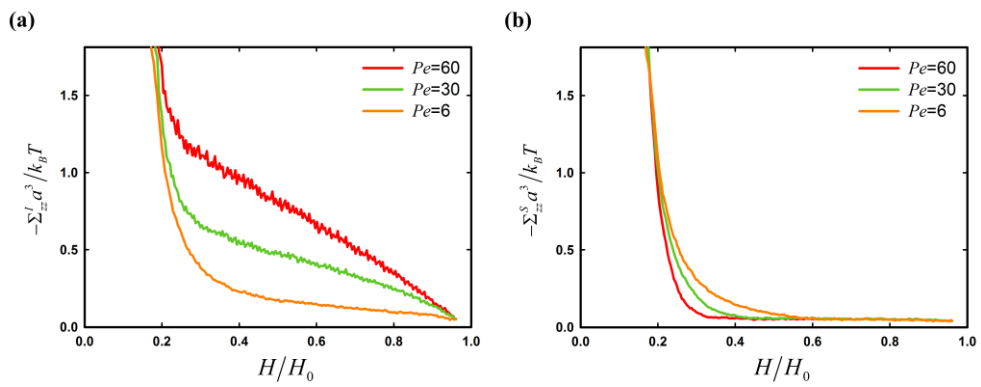


**Figure 2.5** Development of local normal stress at the (a) interface ( $z = H$ ) and (b) substrate ( $z = a$ ).

$$\partial \langle \Sigma_{zz}(z) \rangle / \partial z = \sum_{i=1}^N \langle \delta(z - z_i) f_{iz} \rangle. \quad (2.6)$$

Based on eqn (2.6), we directly observe the correlation of the normal stress difference between the interface and substrate (Figure 2.7) with the net motion of particles (Figure 2.8). Figure 2.7 shows the normal stress difference with the film thickness according to  $Pe$ . The difference is scaled by  $Pen_0k_B T$ , taking into account the increased stress at the interface with the increase in  $Pe$  due to the localization of stress. Here,  $Pen_0k_B T = (\zeta \dot{E}/A)N$ , which means the stress required to move a particle at the given evaporation rate multiplied by the total number of particles. Under this definition, the scaled normal stress difference becomes 1.0 when all the particles are affected by the falling interface.

At high  $Pe$ , such as when the particle diffusion is negligible compared to evaporation, the particles located in the region where the accumulation front just passed are accumulated and pushed down under the influence of the interface. When the interface descends by  $(H_0 - H)/H_0$ , the number of particles proportional to that distance is included in the accumulation region and forced to move downward. Therefore, the scaled normal stress difference is proportional to  $(H_0 - H)/H_0$ , and the slope becomes linear.[69, 70] At  $Pe = 60$ , the slope of the curve is very close to  $-1$  (Figure 2.7). In addition, a larger scaled normal stress difference with decreasing  $Pe$  can be explained by an increase in the thickness of the accumulation region with decreasing  $Pe$ . More particles in the thicker accumulation region are affected by the falling interface,

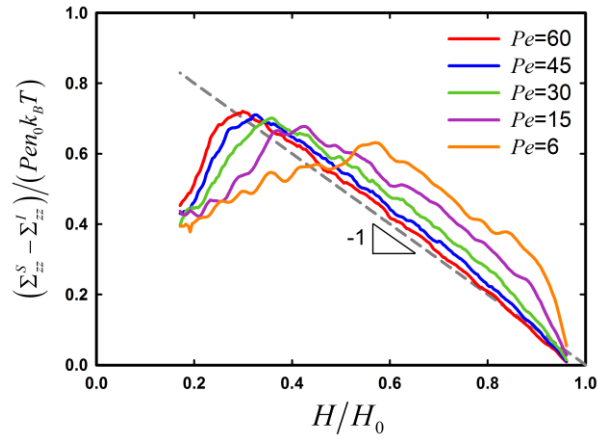


**Figure 2.6** The scaled normal stress difference between the interface and substrate with the film thickness. The gray dotted line represents a guideline with a slope of  $-1$ .

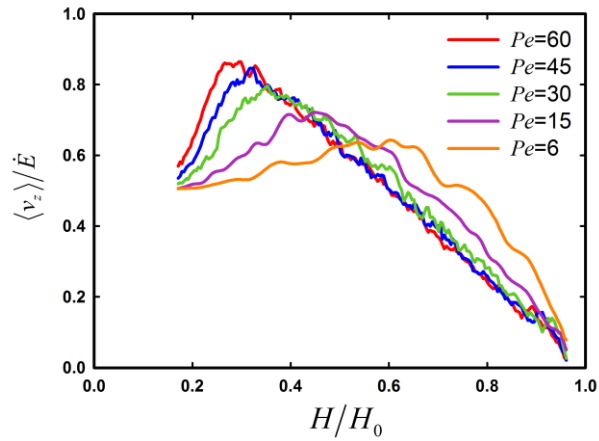


**Figure 2.8** Normalized average particle velocity in the  $z$ -direction with the film thickness. A  $(-)$  sign is used to convert the descending velocity in the  $-z$  direction into a  $(+)$  sign.

which leads to an increase in the scaled normal stress difference.

For all  $Pe$ , the normal stress difference increases as explained above, but finally falls off after the maximum. At higher  $Pe$ , this maximum appears at lower film thickness. Associating with the results of Figures 2.4 and 2.6, the normal stress at the substrate maintains its initial value until the accumulation front reaches the substrate, but the normal stress at the interface increases from the beginning. Naturally, the normal stress difference, which is the difference between the two boundaries, increases. Likewise, when the accumulation front reaches the substrate, the normal stress near the substrate increases rapidly (see Figure 2.6(b)), which leads to a decrease of the normal stress difference. The maximum is observed at  $H/H_0 = 0.58$  for  $Pe = 6$ ,  $H/H_0 = 0.36$  for  $Pe = 30$ , and  $H/H_0 = 0.30$  for  $Pe = 60$ , respectively. It should be noted that for all  $Pe$ , the maximum of the normal stress difference appears at a lower film thickness than that at which the normal stress starts to increase near the substrate. This mismatch indicates that both the drying stage where the accumulation region grows and the stage after the accumulation front contacts the substrate significantly contribute to the stress development. Therefore, the evolution of the normal stress difference and its correlation with the microstructural change should be carefully examined for the latter stage of drying.

As pointed out in eqn (2.6), the average velocity in the  $z$ -direction (vertical direction to the film surface) of all particles is computed to analyze the net motion of the particles. In Figure 2.8, the average velocity normalized by the evaporation rate is observed with the change

in film thickness. As drying proceeds, the velocity increases for all  $Pe$  due to the increasing number of particles affected by the descending interface. At lower  $Pe$ , the normalized average velocity increases faster in the initial stage of drying. This is because not only of the particle motion induced by the interface but also of the particle diffusion toward the substrate direction induced by the volume fraction gradient. In addition, the average velocity decreases after the peak velocity at all tested  $Pe$ . The decrease can be explained as where the downward motion of the particles is significantly hindered by the stationary substrate after the accumulation front contacts the substrate. Interestingly, the average velocity curve according to  $Pe$  is very similar to the scaled normal stress difference curve shown in Figure 2.7. This means that both the evolution of the normal stress difference and the average particle velocity in drying film can be explained by the influence of the interface and the substrate on the particles.

### 2.3.3 Microstructural development

As mentioned previously, the microstructural development in drying film is analyzed to examine a mismatch between the stress difference maximum and the initial stress increase at the substrate. As shown in Figure 2.6, the stress responses are related to the stress evolution at both the interface and substrate, so that the structural analysis needs to be carried out at both boundaries. Here, the contact number of particles at the interface ( $z = H$ ) and substrate ( $z = a$ ) is measured to probe the process of particle accumulation at the interface and the development of microstructure at the substrate. In particular, we focus on the microstructural change that occurs after the accumulation front reaches the substrate. For this purpose, the contact number ( $N_C$ ) is calculated for all particles located at position  $z$  ( $z = H$  or  $a$ ). The number of particles with each contact number is divided by the total number of particles at that position  $z$ . Then, we can get the contact number distribution  $P(z, N_C)$  (in probability function) and analyze the evolution of  $P(z, N_C)$ .

In Figure 2.9(a),  $P(z, N_C)$  at the interface ( $z = H$ ) is shown with the film thickness. At a low evaporation rate of  $Pe = 6$ ,  $N_C$  shows a gradual increase with film drying. On the other hand, at higher  $Pe$ , the increase in  $N_C$  becomes more clear, because the particle accumulation at the interface is further enhanced (Figures 2.2 – 2.4).[71, 72] In this case, the average of  $N_C$  increases and  $P(z, N_C)$  becomes broader. Moreover,  $N_C$  shows a rapid increase at the final stage of drying,  $H/H_0 \leq 0.2$ , regardless of  $Pe$ . This can be explained that at higher particle volume fraction ( $\phi_{\text{bulk}} \geq 0.5$ ), the descent of the interface leads to the compression of the film,



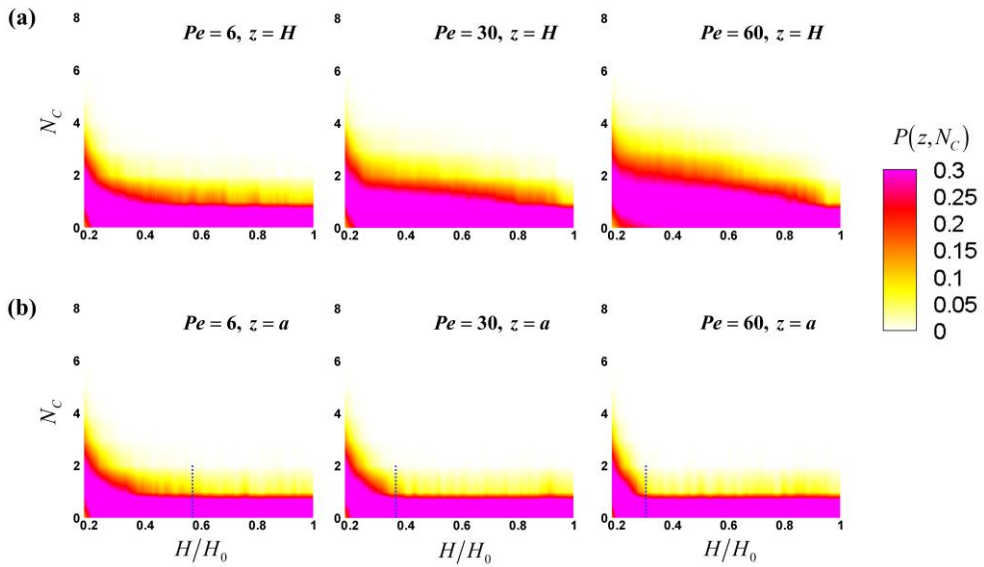


**Figure 2.9** Average contact number distribution of particles  $P(z, N_C)$  at the interface and substrate with film thickness. (a) interface ( $z = H$ ); (b) substrate ( $z = a$ ). The blue dotted line represents the film thickness of the normal stress difference maximum (see Figure 2.7).

which in turn induces a strong increase in  $N_C$ . [72]

In Figure 2.9(b),  $P(z, N_C)$  at the substrate ( $z = a$ ) is shown with the film thickness. At higher  $Pe$ ,  $N_C$  shows a sharp increase at lower film thickness. Note that both before and after the accumulation front reaches the substrate,  $P(z, N_C)$  at the substrate remains unchanged (maintains its initial value) at all  $Pe$ . Interestingly, the film thickness where  $N_C$  increases is nearly identical to the film thickness where the normal stress difference maximum appears (see Figure 2.7). According to these observations, we can correlate the evolution of normal stress and microstructure at the substrate. There is a regime where the contact number distribution hardly changes even though the volume fraction increases after the accumulation front reaches the substrate. As the volume fraction further increases, the contact number begins to increase, which results in a significant increase of normal stress. Consequently, this contributes to a reduction of the normal stress difference. From this analysis, we can confirm that an increase in the particle contact number induces great change in the local normal stress.

In the next step, to examine the microstructural change related to the contact between the particles more closely, the 2D planar pair-distribution function is computed and shown in Figure 2.10 (this analysis is carried out at  $H/H_0 = 0.18$ , where a sufficiently high contact number is observed). First, at  $Pe = 6$ , we observe the planar pair-distribution function in the  $x$ - $y$  plane  $g_{xy}(\mathbf{r}_{xy})$  at the interface and substrate.  $g_{xy}(\mathbf{r}_{xy})$  shows an isotropic pattern at both the interface and substrate and the

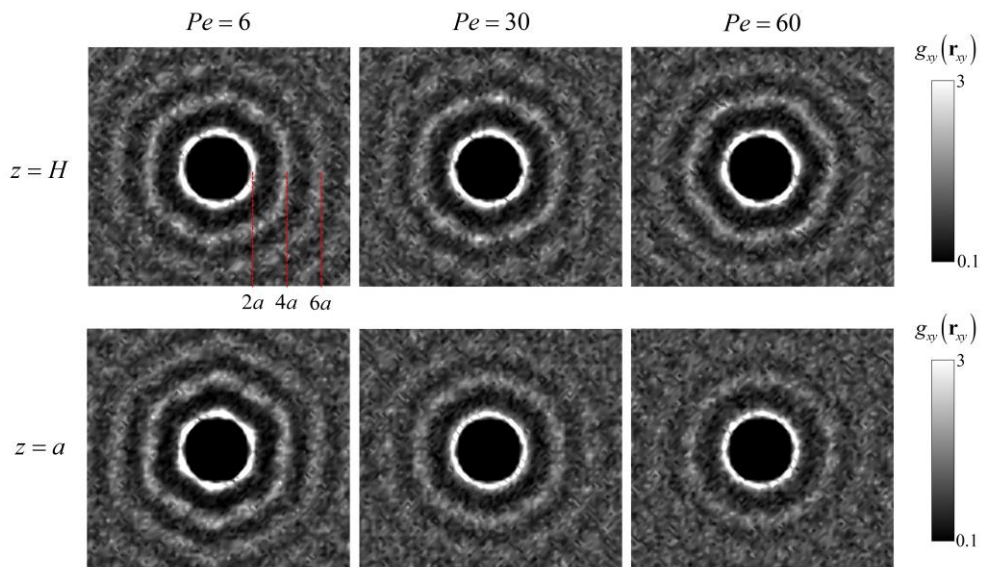


**Figure 2.10** 2D planar pair-distribution function  $g_{xy}(\mathbf{r}_{xy})$  (at  $H/H_0 = 0.18$ ) at the interface ( $z = H$ ) and substrate ( $z = a$ ). Red lines represent  $r_{xy} = 2a$ ,  $4a$ , and  $6a$  from the left, respectively.

high magnitude peaks near  $r_{xy} = 2a, 4a, 6a$  (bright pattern in Figure 2.10) indicate that the particles form an ordered structure. This suggests that microstructural rearrangement can occur sufficiently in a fairly packed film due to a relatively slow evaporation rate.[73, 74] Furthermore,  $g_{xy}(\mathbf{r}_{xy})$  shows more clear hexagonal patterns at the substrate compared to the interface, indicating a more packed structure at the substrate. This can be understood that the descending interface disrupts the rearrangement of the particles, which results in a more disordered structure.

At  $Pe = 30$ , the peak near  $r_{xy} = 6a$  is less clear at the substrate compared to the interface, indicating that a disordered structure is formed. This can be explained with the development of the accumulation region discussed above: particle accumulation occurs at the interface, and the particles in the accumulation region move with the descending interface. The region continuously collects particles so the particle volume fraction gradually increases. Therefore, at the interface, there is enough time for the particles to rearrange in a higher volume fraction, leading to an ordered structure. On the other hand, at the substrate, the volume fraction rapidly increases after the accumulation front reaches the substrate (Figures 2.4 and 2.9). The increase of the local volume fraction occurs in too short a time for the particles to rearrange, thus leading to an increase in the contact number only (with disordered structure). At  $Pe = 60$ , the peak near  $r_{xy} = 6a$  almost disappears and the peak near  $r_{xy} = 4a$  becomes more blurred at the substrate, indicating that a more disordered structure is formed. However, bright and hexagonal

patterns are still observed at the interface. These results show that the structure formation at the substrate can be more sensitive to the drying conditions than that at the interface. At the substrate,  $g_{xy}(\mathbf{r}_{xy})$  shows more clear hexagonal patterns at lower  $Pe$ , indicating a more packed structure at lower  $Pe$ . This demonstrates that the time for the accumulation front to contact the substrate can be a very critical factor in the formation of film structure.

Associating  $g_{xy}(\mathbf{r}_{xy})$  with the evolution of the particle volume fraction and contact number (Figures 2.3, 2.4, and 2.9), a structural development can be drawn. For  $Pe > 1$ , the particles are accumulated at the descending interface, and the particle volume fraction at the interface increases (Figure 2.3). As the distance between particles decreases, the contact between the particles increases, and the ordering of particles begins (Figures 2.9 and 2.10). At higher  $Pe$ , the total drying time decreases so that the total time for particle rearrangement decreases. On the other hand, the particle accumulation at the interface is strongly driven and particle rearrangement occurs from the early stage of drying. Consequently, the microstructure at the interface is influenced by these two factors (Figure 2.10). In contrast, near the substrate, the volume fraction remains unchanged in the beginning. After the accumulation front reaches the substrate, the volume fraction and contact between the particles increase rapidly, and ordering begins. At higher  $Pe$ , the accumulation front reaches the substrate at a lower film thickness, so there is insufficient time for rearrangement to occur, resulting in a

disordered structure.

Although we use an implicit solvent method that does not take into account hydrodynamic interaction, a similar microstructure can be observed in an explicit solvent method. Howard *et al.* studied crystallization kinetics in the drying process of monodisperse colloidal films using the molecular dynamics simulation method.[41] They reported that the hydrodynamic interaction led to an earlier onset of crystal growth, however, the final microstructure was almost identical to the case of the implicit solvent method. These results reveal that the microstructure at the final stage of drying is reasonable in our simulation though hydrodynamic interaction is not considered.

## 2.4 Summary

In this chapter, we investigated the evolution of the normal stress and microstructure in the monodisperse hard-sphere colloidal film drying process by using the Brownian dynamics simulation. When  $Pe > 1$ , the evaporation rate is dominant, and the particles are accumulated at the evaporating interface and the accumulation region grows. The development of the accumulation region is quantified by tracking the accumulation front. The distance between the accumulation front and the interface is larger at lower  $Pe$  at the same film thickness, leading to the accumulation front reaching the substrate much earlier. These accumulated particles localize the stress at the interface, which induces a continuous increase of the stress from the beginning of the drying process. At the substrate, the normal stress first maintains the initial value and then increases with the accumulation front touching the substrate. The influence of the evaporating interface and stationary substrate on stress development has been quantified by the scaled normal stress difference between the two boundaries. Before the accumulation front reaches the substrate, the scaled normal stress difference increases with time due to the normal stress increase at the interface. At high  $Pe$  ( $Pe = 60$ ), all the particles in the region where the accumulation front passed are accumulated and forced to move down with the interface, and accordingly, the scaled normal stress difference increases with the slope of  $-1$ . As  $Pe$  decreases, more particles are affected by the interface at the same film thickness so that the initial scaled normal stress difference is higher. At all  $Pe$  discussed in this

study ( $Pe = 6 - 60$ ), the scaled normal stress difference increases to the maximum, followed by the decrease in the final stage. Interestingly, a mismatch is observed between the stress difference maximum and the initial stress increase at the substrate. This mismatch is explained by the contact number distribution of the particles. At the substrate, the contact number distribution remains unchanged even though the accumulation front reaches the substrate, and then increases as the particle volume fraction further increases. We found that the increase of contact between the particles results in a significant increase of the normal stress, which leads to a decrease in the scaled normal stress difference. In addition, the formation of the accumulation region influences the final structure of the film. As the accumulation front contacts the substrate at low film thickness, the disordered structure is formed due to the limited time for particle rearrangement. So the structure formation at the substrate is more sensitive to  $Pe$  than that at the interface.

In the next chapter, this correlation of the particle distribution during drying with the evolution of the normal stress and microstructure is used to provide insights into the drying process of the bi-disperse colloidal films.



## Chapter 3.

### Drying mechanism of bi-disperse colloidal film

### 3.1 Introduction

In the drying process of bi-disperse colloidal films, modeling approaches have been developed to figure out the changes in particle distribution. Trueman *et al.* performed modeling and explained the large-on-top structure according to the Peclet numbers for the large and small particles, respectively ( $Pe_L = H_0\dot{E}/D_L$ ,  $Pe_S = H_0\dot{E}/D_S$ ).[31] The lower diffusion coefficient of the large particle leads to a higher  $Pe_L$  compared to the  $Pe_S$  of the small particle. This indicates that the evaporation rate is more dominant for the large particle than the small particle, and in turn, the large particles are accumulated at the descending interface. However, this model as well as its extended model considering the interactions between the same species could not explain the small-on-top stratification.[23] Drying models were further extended by considering the influence of different drying conditions, such as particle density and shape, on particle distribution. [19, 75, 76] However, the stratification in colloidal film drying was not considered in these models.

To understand the small-on-top stratification, Fortini *et al.* developed a model by introducing an osmotic pressure.[26] They suggested that the osmotic pressure gradient creates forces that act on the particles away from the interface, and their strength is proportional to the cube of the particle radius. Accordingly, large particles are strongly affected by these forces and the depletion of the large particles occurs near the interface, which leads to the small-on-top structure. But, no quantitative analysis and systematic research have been conducted to

verify this model. In recent years, further extended models have been developed in consideration of the interactions between the particles. Zhou *et al.* derived the forces acting on the two types of particles based on the chemical potential of the dilute hard-sphere mixture.[77] They found that the interaction between the large and small particles creates forces proportional to the cube of each particle radius. As a result, the large particles are pushed downward by the small particles near the interface, resulting in the small-on-top stratification. Zhou *et al.* also derived the conditions for the small-on-top stratification:  $\alpha(\alpha + Pe_L)\phi_s > 1$ , where  $\alpha$  is the size ratio,  $Pe_L$  is the Peclet number for the large particle, and  $\phi_s$  is the volume fraction of the small particles. Recently, Sear and Warren introduced “colloidal diffusiophoresis,” in which the particle motion of one species responds to a volume fraction gradient of another.[69] Similarly, the large particles are pushed downward by the small particles near the interface at high Peclet numbers and volume fractions of the small particles.

The physical models have provided a useful way to capture the reasons and conditions of the stratification; however, it was not possible to observe the stress and microstructure during the drying process. Therefore, the necessity of simulation studies has been emphasized recently. Howard *et al.* described the drying process using the Langevin dynamics simulation method by varying the  $Pe_L$  for the particle size ratio  $\alpha = 4, 6, \text{ and } 8$ .[49] They observed the time evolution of the volume fraction profiles of the large and small particles and showed that the depletion of the large particles near the interface occurred more strongly

at high  $Pe_L$ . Tatsumi *et al.* also performed the Langevin dynamics simulations by varying  $Pe_L$  from 0.1 to 1000 for  $\alpha = 1.5, 2, \text{ and } 4$ , respectively.[78] As a result, they found that there is a  $Pe_L$  where small-on-top stratification is the most enhanced. Most of the previous simulation studies have focused on observing the small-on-top stratification according to the Peclet number.[27, 49, 78–80] There were limitations in the analysis of the stress and microstructure during the drying process and of the origin for the stratification from a microscopic point of view.

In this study, we focus on understanding the small-on-top stratification mechanism during the drying process of bi-disperse colloidal films. To this end, the drying process is described using the Brownian dynamics (BD) simulation. Simulations are performed over a wide range of  $Pe_L$  to observe the change in the stratification dynamics. At the same time, the evolution of the particle distribution and normal stress is observed and analyzed quantitatively. The normal stress difference between the interface and the substrate is carefully investigated, and the direct correlation between the normal stress difference and microstructural development is examined. As a result, the normal stress and its correlation with microstructure guide us to examine the drying mechanism of bi-disperse colloidal films and the stratification mechanism.

## 3.2 Simulation methods

### 3.2.1 Model system

The model system is set to deal with the drying process of bi-disperse colloidal films. Hard-sphere colloidal particles with two different sizes of  $0.5$  and  $0.125\mu\text{m}$  radius are dispersed in a Newtonian fluid. The initial bulk volume fraction is  $\phi_{\text{bulk},0} = 0.1$ . The initial film thickness is  $30\mu\text{m}$ , and the drying proceeds at a constant evaporation rate (the rate of decrease in the interface position). To observe the change in the drying process with the occurrence of the stratification, drying is performed under various evaporation rates ( $5\text{--}50\mu\text{m}/\text{min}$ ). These drying conditions are similar to the actual drying process of silica colloidal film in air (evaporation rate  $2\text{--}80\mu\text{m}/\text{min}$ ). [19]

The assumptions of the drying simulation are based on that of the drying model of bi-disperse colloidal films. [77] The model assumed the constant evaporation rate during drying, thin film that the lateral direction was not important, and no bulk flow in the film. Under these assumptions, the model proposed that the evolution of the volume fraction profile was influenced by the Peclet number for the large and small particles, particle size ratio, and initial volume fraction of the large and small particles. In this study, we focused on the effect of the Peclet number on the drying mechanism of bi-disperse colloidal films.

Figure 3.1 illustrates the three-dimensional (3D) simulation domain based on the model system. A bi-disperse colloidal film is coated on a stationary planar substrate ( $z = 0$ ). Hard-sphere particles with two

different sizes are initially randomly dispersed, and the ratio between the large particle radius  $a_L$  and small  $a_S$  is 4:1 (size ratio  $\alpha = 4$ ). The diffusion coefficient of the small particle is four times larger than that of the large particle ( $D_S = \alpha D_L$ ) from the Einstein–Stokes relationship,  $D = k_B T / 6\pi\eta a$ . The initial volume fraction of the large particles is  $\phi_{L,0} = 0.07$  (the number of particles  $N_L = 1500$ ) and of the small particles is  $\phi_{S,0} = 0.03$  (the number of particles  $N_S = 40000$ ). The domain size in the  $x$  and  $y$ -direction is  $40a_L$ , and periodic boundary conditions are applied. The initial film thickness is  $H_0 = 60a_L$ , and the interface moves down to the  $-z$  direction at a constant evaporation rate during drying. The evaporation rates are set to  $\dot{E} = 6, 30, \text{ and } 60 H_0/\tau_L$ , which corresponds to the Peclet numbers  $Pe_L (= H_0\dot{E}/D_L) = 6, 30, \text{ and } 60$  for the large particle ( $Pe_S = H_0\dot{E}/D_S = 1.5, 7.5, \text{ and } 15$  for the small particle). Drying proceeds to the film thickness  $H = 0.18H_0$ , and at this point, the bulk volume fraction reaches  $\phi_{\text{bulk}} = 0.55$ . Ten simulations are conducted with different starting configurations for each  $Pe_L$ .

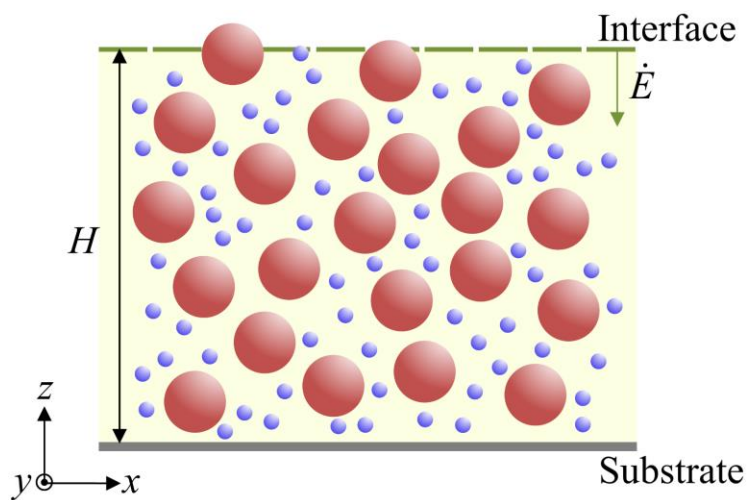


**Figure 3.1** Schematic diagram of the bi-disperse colloidal film drying. The large particles are colored in red, and small in blue.

### 3.2.2 Brownian Dynamics (BD) simulation

The behavior of the particles in the colloidal film is described by using the Brownian dynamics (BD) simulation.[43, 44] The governing equation is the overdamped Langevin equation

$$\mathbf{0} = -\zeta_i \dot{\mathbf{r}}_i + \mathbf{f}_i^P + \mathbf{f}_i^S + \mathbf{f}_i^I + \mathbf{f}_i^B. \quad (3.1)$$

In the above equation, the first term on the right-hand side is the hydrodynamic force described by the Stokes drag force (Stokes friction  $\zeta_i = 6\pi\eta a_i$ ).  $\mathbf{f}_i^P$  is the inter-particle force,  $\mathbf{f}_i^S$  is the force from the substrate, and  $\mathbf{f}_i^I$  is the capillary force at the interface. These forces are calculated by the differentiation of the potentials. Here,  $\mathbf{f}_i^P = -\sum_j \partial U_{ij}^P / \partial \mathbf{x}_i$  from the inter-particle potential ( $U_{ij}^P$ ) between the different particles  $i$  and  $j$ .  $\mathbf{f}_i^S = -\partial U_i^S / \partial \mathbf{x}_i$  from the particle-wall potential ( $U_i^S$ ) and  $\mathbf{f}_i^I = -\partial U_i^I / \partial \mathbf{x}_i$  from the particle-interface potential ( $U_i^I$ ).  $\mathbf{f}_i^B$  is the Brownian force, which is generated as a random value with zero mean and variance  $\langle \mathbf{f}_i^B(t) \mathbf{f}_i^B(t') \rangle = 2\zeta_i k_B T \delta(t-t') \mathbf{I}$ . Eqn (3.1) is numerically solved by the Euler method over the time step  $\Delta t = 10^{-8} H_0^2 / D_L$ . [45] This time step is small enough to prevent the overlap between the particles.



### 3.2.3 Interaction potential

The interaction between the particles is modeled using the Weeks–Chandler–Andersen (WCA) type potential (96–48). The potential between the particles  $i$  and  $j$  is as follows

$$U_{ij}^P(r_{ij}) = \begin{cases} 4\varepsilon \left[ \left( \frac{\sigma_{ij}}{r_{ij}} \right)^{96} - \left( \frac{\sigma_{ij}}{r_{ij}} \right)^{48} + \frac{1}{4} \right] & r_{ij} < 2^{1/48} \sigma_{ij} \\ 0 & r_{ij} > 2^{1/48} \sigma_{ij} \end{cases} \quad (3.2)$$

where  $r_{ij}$  is the center-to-center distance between the two particles and  $\sigma_{ij} = a_i + a_j$  is the effective diameter ( $a_i$  is the radius of particle  $i$ ).  $\varepsilon$  represents the strength of repulsion and is set to be  $\varepsilon = k_B T$ .

The substrate acts as a (nearly) hard wall and the interaction between the particle and substrate is also modeled using the Weeks–Chandler–Andersen (WCA) type potential (96–48) [51, 52]

$$U_i^S(z_i) = \begin{cases} 4\varepsilon \left[ \left( \frac{\sigma_{ii}}{z_i + a_i} \right)^{96} - \left( \frac{\sigma_{ii}}{z_i + a_i} \right)^{48} + \frac{1}{4} \right] & z_i + a_i < 2^{1/48} \sigma_{ii} \\ 0 & z_i + a_i > 2^{1/48} \sigma_{ii} \end{cases} \quad (3.3)$$

In this potential, the particle  $i$  is repelled by an imaginary wall particle (radius  $a_i$ ) located at a distance  $a_i$  from the substrate  $z = 0$  in the  $-z$  direction. [51, 52] Here,  $z_i$  is the height of the center of particle  $i$  above the substrate.

The interaction between the particle and soft film interface is modeled using the purely repulsive harmonic potential. [26, 49]

$$U_i^I(z_i) = \begin{cases} 0 & z_i < H \\ \kappa_i(z_i - H)^2 / 2 & H \leq z_i < H_i^c \\ \kappa_i(H_i^c - H)^2 / 2 - F_i^g(z_i - H_i^c) & z_i \geq H_i^c \end{cases} \quad (3.4)$$

Here,  $\kappa_i$  is a spring constant to capture the strength of the interfacial tension acting on particle  $i$ . The interfacial tension is proportional to the particle surface area so that the spring constant for the large and small particle is scaled accordingly,  $\kappa_L/\kappa_S = (a_L/a_S)^2 = \alpha^2$ . [49, 55] We take the spring constant for the large particle  $\kappa_L = 1000\epsilon/a_L^2$ , an appropriate value for numerical stability and for moving particles along with the interface.  $H_i^c = H + a_i$  is a cutoff height where a particle is completely above the interface and begins to descend by gravity,  $F_i^g$ .  $F_i^g = -\kappa_i(H_i^c - H)$  is set to ensure that the capillary force is continuous at  $z_i = H_i^c$ . In this potential, the particles in  $H \leq z_i < H_i^c$  descend by the force proportional to  $z_i - H$ , and descend by  $F_i^g$  in  $z_i > H_i^c$ .

### 3.2.4 Normal stress calculation

The local normal stress in the  $z$ -direction,  $\Sigma_{zz}(z)$ , is calculated using the method of planes (MOP).[56, 57] The expression is as follows

$$\begin{aligned} \langle \Sigma_{zz}(z) \rangle = & -\langle n_L(z) \rangle k_B T - \langle n_S(z) \rangle k_B T \\ & - \frac{1}{2A} \left\langle \sum_{i=1}^{N_L} f_{iz}^P \operatorname{sgn}(z_i - z) \right\rangle - \frac{1}{2A} \left\langle \sum_{j=1}^{N_S} f_{jz}^P \operatorname{sgn}(z_j - z) \right\rangle \end{aligned} \quad (3.5)$$

where  $\langle \cdot \rangle$  denotes an ensemble average and  $n_L(z)$  and  $n_S(z)$  are the local number density of the large and small particles, respectively.  $A$  is the cross-sectional ( $x$ - $y$  plane) area of the simulation domain, and  $f_{iz}^P$  is the  $z$  component of the total inter-particle force acting on particle  $i$ .  $\operatorname{sgn}(\cdot)$  denotes a sign operator, which gives the value 1 or  $-1$  when the input is positive or negative, respectively. The first two terms in eqn (3.5),  $-\langle n(z) \rangle k_B T$ , are the normal stress associated with the thermal energy of the Brownian particles, and the other two terms,  $-\frac{1}{2A} \left\langle \sum_{i=1}^N f_{iz}^P \operatorname{sgn}(z_i - z) \right\rangle$ , are the inter-particle stress, which originates from the inter-particle forces. The inter-particle stress considers all of the contributions of the inter-particle forces ( $f_{iz}^P$ ) on the local position  $z$ , so that it is advantageous to reduce the noise compared to spatial binning.[56] The effects of hydrodynamic interactions and the forces from the interface and substrate are not reflected to calculate the stress.

## 3.3 Results and discussion

### 3.3.1 Particle distribution in drying film

First, the particle distribution in drying films is visually observed according to the Peclet number ( $Pe_L$ ). Figure 3.2 shows the snapshots of the drying process of bi-disperse colloidal films. In this figure, the large particles are colored in red and small in blue. The film thickness ( $H$ ) is denoted normalized by the initial film thickness ( $H_0$ ), which decreases with time from the initial value of 1.0. When  $Pe_L = 6$  in Figure 3.2(a), the number of large particles at the interface increases as drying progresses. Accordingly, at  $H/H_0 = 0.4$ , a layer dominated by the large particles is formed at the interface. As the large particles inside the film approach the interface during the drying process, these particles are continuously trapped to form a layer.[49] At  $H/H_0 = 0.2$ , close to the final stage of drying, the large and small particles are distributed throughout the film, so we can confirm that small-on-top stratification does not occur at  $Pe_L = 6$ . When  $Pe_L = 60$  in Figure 3.2(b), a stratified layer composed of only small particles is formed below the interface. The thickness of the stratified layer is thicker at  $H/H_0 = 0.4$  than any other film thickness. At  $H/H_0 = 0.2$ , the number of large particles at the interface is less than that in  $Pe_L = 6$ , which indicates that the large particles initially located near the interface are pushed down to the substrate during drying.

These results are similar to the simulation results of Howard *et al.*[49] They observed the distribution of large and small particles (size ratio  $\alpha = 4$ ) at the final dried film when  $Pe_L = 12$  and 120. When  $Pe_L = 12$ ,

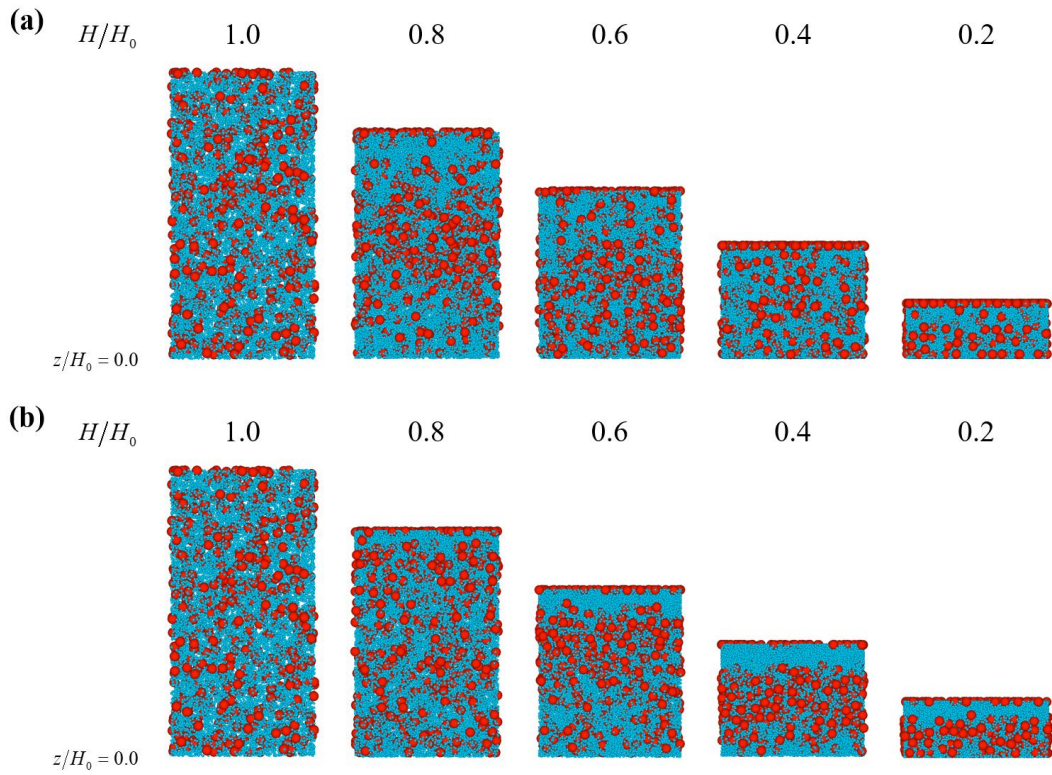


**Figure 3.2** Snapshots of the particle configuration in drying films. (a)  $Pe_L = 6$ ; (b)  $Pe_L = 60$ .

stratification did not occur, and the large particles were trapped at the interface to form a layer. When  $Pe_L = 120$ , the small-on-top structure was formed and some of the large particles were located at the interface. Furthermore, our results can be verified with the experimental results of Liu *et al.* [81] They observed the particle composition at the top surface (interface) of the final dried film by varying  $Pe_L$ . They found that some large particles were trapped at the top surface, and the number of large particles decreased as  $Pe_L$  increased. These simulation and experimental results can be related to our observations at  $Pe_L = 6$  and 60, which shows the change in particle distribution depending on the occurrence of small-on-top stratification (Figure 3.2).

Next, the time evolution of the particle distribution is quantitatively investigated during the drying process. Figure 3.3 shows the local volume fraction profile of the large and small particles according to the film thickness,  $H/H_0$ . The volume fraction from the substrate ( $z = a_L$ ) to the film thickness ( $z = H$ ) is plotted for each film thickness, and the location of the interface is  $z/H_0 = H/H_0$  for the corresponding film thickness. In this analysis, the  $z$ -axis ( $z/H_0$ ) bin width is fixed at  $0.02a_L$ , and the results are averaged over ten different initial configurations (Note that the volume fraction profile in  $H/H_0 > 0.96$  is omitted because insufficient particle number density produces a large noise at the interface. In addition, the local volume fraction in  $z < a_L$  is also omitted for the same reason.).

Let us begin with the volume fraction profile at  $Pe_L = 6$  (Figure 3.3). At the interface, the volume fraction of the large particles increases with

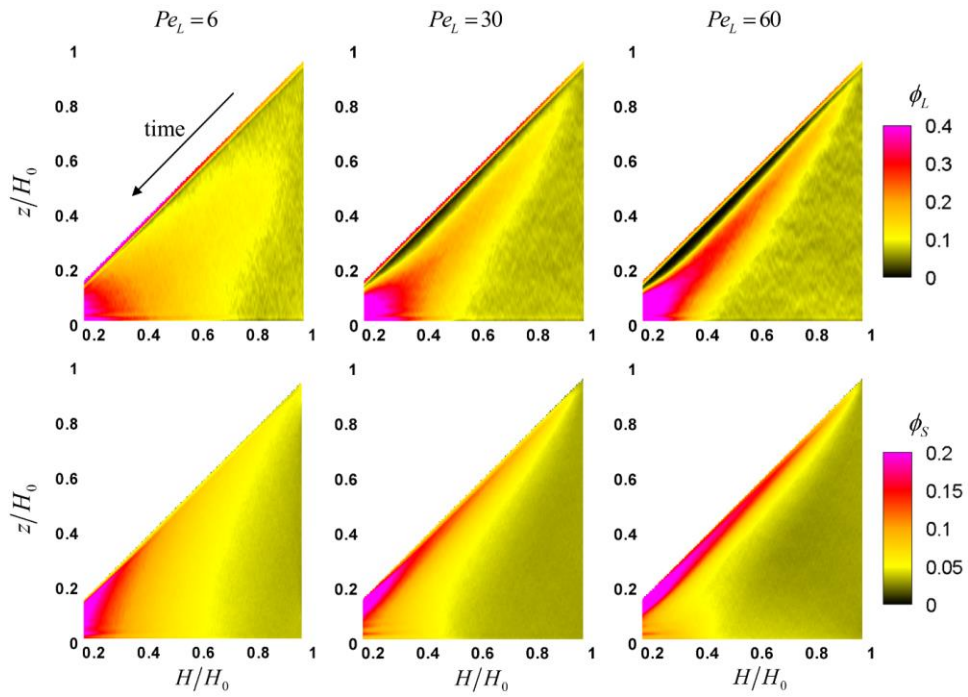


**Figure 3.3** Local volume fraction profile of the large and small particles during drying. The volume fraction from the substrate ( $z = a_L$ ) to the interface ( $z = H$ ) is shown at the corresponding film thickness.

time, but that of the small particles remains at the initial low value during drying. Near the substrate, the volume fraction of both particles maintains the initial volume fraction for  $H/H_0 \geq 0.7$  and then increases as the film thickness decreases for  $H/H_0 < 0.7$ . In the film, the volume fraction of both particles is higher near the interface than that at the substrate in the initial stage of drying. When  $Pe_L, Pe_S > 1$ , where evaporation is more dominant than diffusion, the particles are accumulated at the descending interface, resulting in a higher volume fraction at the interface.[19, 29, 63] To quantify the accumulation of the particles, we define that the position ( $z$ ) is included in the accumulation region when either the volume fraction of the large or small particles at ( $z$ ) increases by more than 10% of its initial volume fraction ( $\phi_{L,0} = 0.07$ ,  $\phi_{S,0} = 0.03$ ). In this case, the accumulation region at  $H/H_0 = 0.8$  appears in  $z/H_0 > 0.27$ . Interestingly, the volume fraction of the large particles in the accumulation region is lower close to the interface. This is because the large particles are trapped at the interface during drying and only a few large particles can exist below the interface.

When  $H/H_0 = 30$ , at the interface, the volume fraction of the large particles increases with time for  $H/H_0 > 0.8$  and remains constant for  $H/H_0 < 0.8$ . Below the interface, the volume fraction of the large particles clearly shows a lower value compared to the surroundings. As the film thickness decreases, the volume fraction in this region decreases and finally becomes zero. On the other hand, the volume fraction of the small particles is high in this region, which indicates that the stratified layer of small particles is formed. Based on these observations, the particle



distribution near the interface can be correlated with the formation of the stratified layer. The stratified layer prevents the large particles from accessing or escaping the interface so that the volume fraction of the large particles at the interface remains constant for  $H/H_0 < 0.8$ . Furthermore, the large particles form an accumulation region below the stratified layer (i.e.,  $0.41 < z/H_0 < 0.67$  at  $H/H_0 = 0.7$ ). In this accumulation region, the volume fraction of the large particles increases with time, which means the region collects more large particles along with its descent. For the small particles, however, the volume fraction is the highest at the interface and decreases toward the substrate. This indicates that the small particles are accumulated at the interface, different from the large particles. At the substrate, the volume fraction of both particles increases when  $H/H_0 < 0.5$ .

Compared with  $Pe_L = 30$ , when  $Pe_L = 60$ , a more pronounced stratified layer is formed near the interface, which means that the depletion of the large particles is driven more strongly. Accordingly, the volume fraction of the large particles is lower at the interface. In the accumulation region, the volume fraction of the large particles is higher and its thickness is lower at the same film thickness (i.e.,  $0.46 < z/H_0 < 0.66$  at  $H/H_0 = 0.7$ ). This is qualitatively expected because at higher  $Pe_L$ , a shorter time is needed to be dried to a specific film thickness, and in turn, the accumulated particles cannot diffuse far away from the interface. For the same reason, the volume fraction of the small particles is higher at the interface. At the substrate, the volume fraction of both particles increases when  $H/H_0 < 0.4$ .

These observations fit fairly well to the prediction of Zhou *et al.* [77]. They proposed a stratification model for the hard-sphere mixture based on the chemical potential gradient. They revealed that the small-on-top stratification occurred if  $\alpha(\alpha + Pe_L)\phi_s > 1$ . In this study,  $\alpha(\alpha + Pe_L)\phi_s = 7.7$  for  $Pe_L = 60$ , 4.1 for  $Pe_L = 30$ , and 1.2 for  $Pe_L = 6$ . Thus, our simulation is in line with the stratification regime proposed by Zhou *et al.* at high  $Pe_L$ . A little mismatch at  $Pe_L = 6$  where the stratification does not occur in this study can be due to the dilute mixture assumption used in their model. The model seems to miss some drying mechanics in a wide range of volume fractions of the colloidal film, which is covered in our simulation.

The development of the accumulation region is closely examined. As quantification of accumulation, the position  $z$  of the accumulation front is computed with the minimum  $z$ -coordinates in the accumulation region. In Figure 3.4, the position of the accumulation front is plotted with the position of the interface according to the film thickness. In all  $Pe_L$  tested in this study, the distance between the interface and accumulation front increases as the film thickness decreases. At the same film thickness, this gap is greater for the lower  $Pe_L$ . For example, at  $H/H_0 = 0.8$ , this gap is  $0.53H_0$  for  $Pe_L = 6$ ,  $0.30H_0$  for  $Pe_L = 30$ , and  $0.23H_0$  for  $Pe_L = 60$ . This result also indicates that the particles in the accumulation region can diffuse longer distances toward the substrate for the lower  $Pe_L$ . At the substrate, the accumulation front touches the substrate at thicker film thickness for the lower  $Pe_L$ . This film thickness is  $H/H_0 = 0.70$  for  $Pe_L = 6$ ,  $H/H_0 = 0.51$  for  $Pe_L = 30$ , and  $H/H_0 = 0.42$  for  $Pe_L = 60$ . (Note that the

accumulation front is defined based on the local volume fraction so that it is not defined below the height of  $a_L$ . Accordingly, the lines do not go to 0 but only to the height of  $a_L$ .)

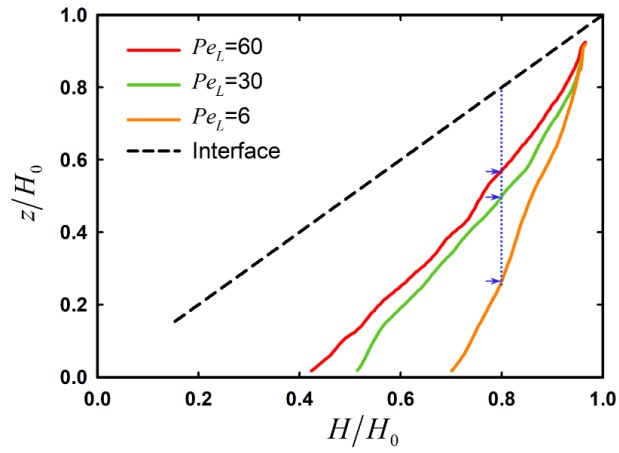


**Figure 3.4** Position  $z$  of accumulation front along the normalized film thickness ( $H/H_0$ ). The blue dotted line and arrows show the thickness of the accumulation region at  $H/H_0 = 0.8$ .

### 3.3.2 Normal stress localization in drying film

Figure 3.5 shows the local normal stress profile during the drying process. The corresponding  $H/H_0$  is denoted next to the profile. Moreover, the time evolution of the normal stress is shown at the interface. This stress is calculated by an extrapolation of the local normal stress evaluated near the interface to the position of the interface. Note that for the same reason in the local volume fraction profile (Figure 3.3), the normal stress in  $H/H_0 > 0.96$  and in  $z < a_L$  are not plotted.

The local normal stress profile is monitored according to the  $Pe_L$ . At  $Pe_L = 6$  (Figure 3.5(a)), the normal stress difference across the film is small during drying. This can be understood that the motion of the particles considerably stabilizes the perturbation of the normal stress due to the moving interface.[40] Interestingly, the local volume fraction profile shows variations with position  $z$  (see Figure 3.3) in contrast to the almost uniform profile of the normal stress. Therefore, we can confirm that not only particle distribution but also stress development must be considered to understand the drying process of bi-disperse colloidal films. At high  $Pe_L$  (Figures 3.5(b), (c)), the normal stress difference between the interface and substrate becomes larger, suggesting that more dominant evaporation limits the stabilization of the normal stress, and in turn, the stress is localized at the interface.[64–66] Moreover, the normal stress at the interface is higher for  $Pe_L = 60$  than that for  $Pe_L = 30$  at the same film thickness. This is also due to the effect of the faster evaporation rate.

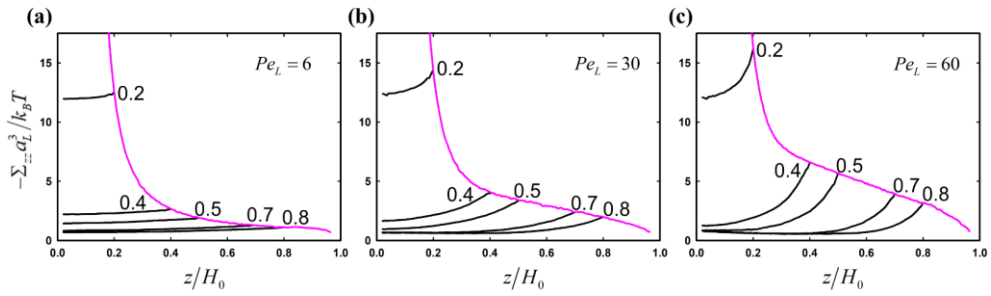


**Figure 3.5** Evolution of the local normal stress during drying. (a)  $Pe_L = 6$ ; (b)  $Pe_L = 30$ ; (c)  $Pe_L = 60$ . The local normal stress profile is shown in a black solid line, and the normal stress at the interface is shown in pink.  $H/H_0$  is denoted next to the corresponding local normal stress profile.

In Figure 3.5, a different stress evolution is observed at the two boundaries. For all  $Pe_L$ , at the interface, the normal stress continuously increases from the beginning as the film thickness decreases. On the other hand, at the substrate, the normal stress remains at the initial value even when the drying is in progress (i.e.,  $H/H_0 = 0.8$ ), and the normal stress at the substrate begins to increase at lower film thickness for higher  $Pe_L$ . The film thickness of the initial stress increase is  $H/H_0 \sim 0.7$  for  $Pe_L = 6$ ,  $H/H_0 \sim 0.5$  for  $Pe_L = 30$ , and  $H/H_0 \sim 0.4$  for  $Pe_L = 60$ . Interestingly, this film thickness is almost identical to the film thickness when the accumulation front touches the substrate (see Figure 3.4). These results suggest that the development of the normal stress is further enhanced when the accumulation front contacts the substrate. In addition, at all  $Pe_L$ , the normal stress increases considerably for  $H/H_0 \leq 0.4$ . This is a drying stage after the accumulation front contacts the substrate and the volume fraction increases with time. Furthermore, in  $H/H_0 \leq 0.4$ , the bulk particle volume fraction is high ( $\phi_{\text{bulk}} \geq 0.25$ ) and increases rapidly as drying proceeds, which results in the acceleration of the normal stress development.

The high normal stress reflects a strong expansion outward of the particle structure.[59] This implies that the particles experience the force toward the substrate under the normal stress profile decreasing from the interface to the substrate. Based on this hypothesis, we examine the correspondence between the normal stress difference formed in the film (Figure 3.6) and the net motion of large and small particles (Figure 3.7). Figure 3.6 shows the evolution of the normal

stress difference between the interface and substrate according to  $Pe_L$ . The normal stress difference is scaled to consider the stress increase with increasing  $Pe_L$  ( $Pe_S$ ) due to stress localization. The scaling factor is given in the form

$$Pe_{eff}n_0k_B T = (Pe_L n_L + Pe_S n_S)k_B T = (\zeta_L \dot{E}/A)N_L + (\zeta_S \dot{E}/A)N_S \quad (3.6)$$

where,  $n_0$  is the initial number density of the total particles.  $Pe_k n_k k_B T = (\zeta_k \dot{E}/A)N_k$  ( $k = L, S$ ) represents the stress required to move a type  $k$  particle at the evaporation rate ( $\zeta_k \dot{E}/A$ ) multiplied by the total number of type  $k$  particles,  $N_k$ . Under this definition, when all of the particles are forced down by the descending interface, the scaled normal stress difference becomes 1.0. In addition, the evolution of the scaled normal stress difference in the drying process of monodisperse colloidal film (Figure 2.7) is also plotted in Figure 3.6. In the monodisperse colloidal film system, the particle radius  $a = a_L$ , initial volume fraction  $\phi_0 = 0.1$  (the number of particles  $N = 2,000$ ), and other conditions are the same as in the bi-disperse colloidal film system.

In Figure 3.6, the scaled normal stress difference increases from the beginning for all  $Pe_L$ . Associating with the results in Figure 3.5, the normal stress at the interface increases during drying but at the substrate retains the initial value for a while. Naturally, an increase in the normal stress difference can be expected. This increasing scaled difference shows a larger value for lower  $Pe_L$ . In addition, the difference reaches a maximum at higher film thicknesses for lower  $Pe_L$ . The maximum is observed at  $H/H_0 \sim 0.7$  for  $Pe_L = 6$ ,  $H/H_0 \sim 0.5$  for  $Pe_L = 30$ ,



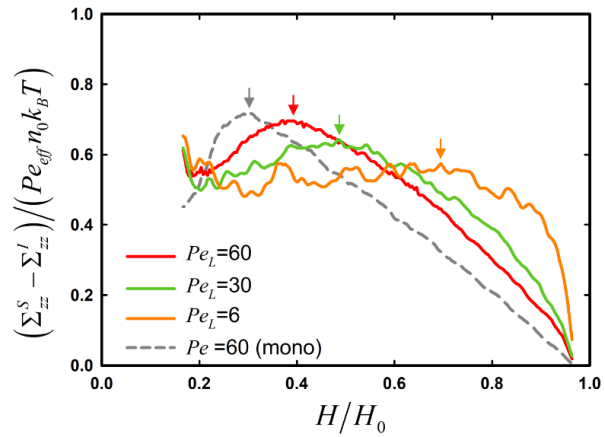


**Figure 3.6** Evolution of the scaled normal stress difference between the interface and substrate. The scaled normal stress difference observed in the monodisperse colloidal film is shown in a gray dotted line. The arrows indicate the maximum of each curve.

and  $H/H_0 \sim 0.4$  for  $Pe_L = 60$ . It should be noted that this film thickness is similar to the film thickness where the accumulation front touches the substrate (Figure 3.4) and the normal stress begins to increase at the substrate (Figure 3.5). Thus, the scaled normal stress difference can be correlated with the formation of the accumulation front. At lower  $Pe_L$ , the thickness of the accumulation region is larger at the same film thickness. This can be understood that the total proportion of the particles affected by the interface is larger, which leads to the higher scaled normal stress difference.

After the maximum, the scaled normal stress difference decreases for  $Pe_L = 30$  and  $60$ . On the other hand, the difference remains almost constant for  $Pe_L = 6$ , which suggests that the normal stress evenly increases throughout the film during drying (see Figure 3.5(a)). Furthermore, in all  $Pe_L$ , the difference increases again in the final stage of drying as in  $H/H_0 < 0.2$ . Note that the reason for this increase is different from the increase at the initial stage of drying. The increase in the beginning is originated from the formation of the accumulation region, and accordingly, the localization of the normal stress at the interface. However, in  $H/H_0 < 0.2$ , the accumulation front has already reached the substrate, and the stress localization occurs at the interface in the regime where the volume fraction is very high ( $\phi_{\text{bulk}} \geq 0.5$ ). Therefore, the microstructural analysis and its correlation with the stress localization are required to understand the origin of the normal stress difference increase. Also, this analysis is carried out in the next section.

Next, the development of the scaled normal stress difference in the

bi-disperse film ( $Pe_L = 60$ ) is compared with the monodisperse film ( $Pe = 60$ ) to understand the change in stress development (Figure 3.6). In the monodisperse film at  $Pe = 60$ , the particles contacting with the accumulation front are included in the accumulation region. So, the number of particles in the accumulation region is proportional to the distance where the accumulation front passes, resulting in a linear increase of the scaled normal stress difference along the film thickness. After the accumulation front touches the substrate ( $H/H_0 \sim 0.3$ ), a rapid normal stress increase at the substrate leads to a decrease in the stress difference. In the bi-disperse film, compared to the monodisperse film, the scaled normal stress difference is higher at the same film thickness before it decreases. Also, the difference reaches the maximum at higher film thicknesses. These results imply that in the bi-disperse film, more particles are influenced by the descending interface and a thicker accumulation region is formed at the same film thickness. A thicker accumulation region results in the accumulation front touching the substrate at the early stage (higher film thickness), and the maximum appears at a higher film thickness. Furthermore, the increase in the scaled normal stress difference in  $H/H_0 < 0.2$  is only observed in the bi-disperse film.

As mentioned before, the average particle velocity in the  $z$ -direction is computed to observe the net motion of the particles. The average velocity is obtained for each type of particle to examine the effect of the stratification. Figure 3.7 shows the evolution of the average velocity normalized by the evaporation rate ( $-\langle v_z \rangle / \dot{E}$ ). Note that a  $(-)$  sign is

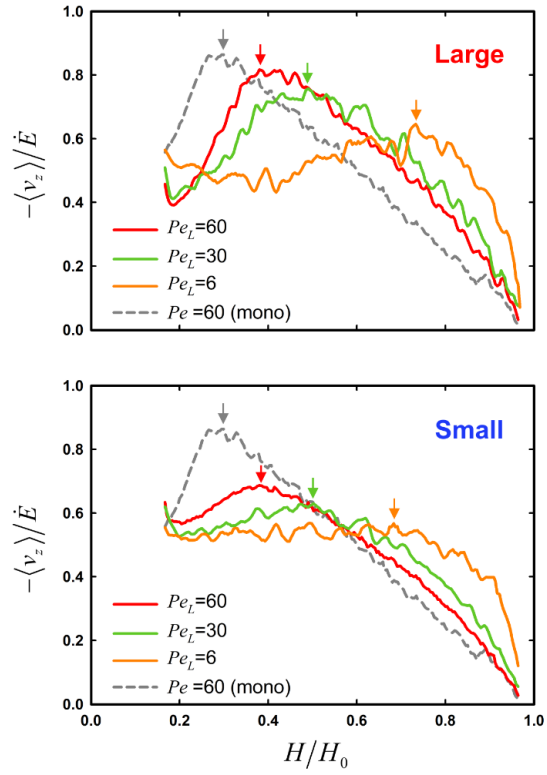


**Figure 3.7** Evolution of the normalized average velocity in the  $z$ -direction for each type of particle. The normalized average velocity in the monodisperse colloidal film is shown in a gray dotted line. The arrows indicate the maximum of each curve. A  $(-)$  sign is used to convert the descending velocity in the  $-z$  direction into a  $(+)$  sign.

used to convert the velocity in the  $-z$  direction into a (+) sign (because the descending interface is in the  $-z$  direction, i.e., the evaporation rate is expressed as a (+) sign). In addition, the normalized average particle velocity observed in the monodisperse film is also shown in the same figure (Figure 2.8).

The normalized average velocity according to  $Pe_L$  (Figure 3.7) shares a similarity with the scaled normal stress difference (Figure 3.6). In all  $Pe_L$ , the normalized average velocity increases ( $-\langle v_z \rangle / \dot{E}$  increases) from the beginning for both the large and small particles. For lower  $Pe_L$ , the normalized average velocity shows a larger value in the initial stage. This can be understood that as drying progresses, the number of particles affected by the descending interface increases, leading to an increase in the average velocity. In addition, the diffusive motion drives the particles in the  $-z$  direction to resolve the volume fraction gradient, which induces higher scaled velocity for lower  $Pe_L$ . After the maximum, the average velocity of the large particle decreases for all  $Pe_L$ . This is similar to the small particles for  $Pe_L \geq 30$ . The decrease after the maximum can arise from the stationary substrate, which significantly hinders the particle motion in the  $-z$  direction after the accumulation front touches the substrate. However, at  $Pe_L = 6$ , the average velocity of the small particle is almost constant for  $H/H_0 < 0.7$ . We emphasize that constant average velocity can be related to the constant normal stress difference in  $H/H_0 < 0.7$  (see Figure 3.6), and the microstructural analysis is necessary to explain it. Furthermore, at all  $Pe_L$ , the average velocity increases again in  $H/H_0 < 0.2$  for both types of particles. This is

also associated with an increase in the normal stress difference in  $H/H_0 < 0.2$ .

The normalized average velocity in the bi-disperse film ( $Pe_L = 60$ ) is compared with that in the monodisperse film ( $Pe = 60$ ) (Figure 3.7). In the monodisperse film, the normalized average velocity increases until the accumulation front touches the substrate and then decreases in the final stage of drying. In the bi-disperse film, the normalized average velocity increases faster for both the large and small particles than for the monodisperse particles, and the average is higher for the large than that for the small (i.e.,  $-\langle v_z \rangle / \dot{E} = 0.51$  for large, 0.43 for small, and 0.37 for monodisperse particles at  $H/H_0 = 0.7$ ). This result can be explained in relation to the small-on-top stratification. When the stratification occurs, the large particles are pushed down near the interface, while the small particles are accumulated at the interface. Therefore, the average velocity of the large particles can be predicted higher than that of the small particles. In addition, the proportion of the number of particles that are affected by the interface is higher for both the large and small particles than that for the monodisperse particles (Figure 3.6), leading to a higher average velocity. Interestingly, after reaching the maximum, the amount of velocity decrease of the monodisperse particle (from the peak to the bottom) is lower than that of the large particle and higher than that of the small particle (i.e.,  $\Delta \langle v_z \rangle / \dot{E} = 0.41$  for large, 0.11 for small, and 0.30 for monodisperse particle). This is also related to the small-on-top stratification. A relatively higher proportion of the large particles is located near the substrate due to the depletion near the interface. On

the other hand, the small particles are accumulated at the interface and a relatively lower proportion of the small particles is located near the substrate. Therefore, the decrease in the average velocity due to the stationary substrate is higher for the large particle and lower for the small particle than that for the monodisperse particle.

In the previous studies, the motion of the particle has been correlated to the normal stress profile. For example, several simulation studies focused on the analysis of the normal stress profile to investigate a shear-induced size segregation of bi-disperse colloidal suspension. [82–84] They reported that the different effects of the normal stress on the different types of particles can induce the size segregation and qualitatively examined the relationship between the normal stress and particle motion. Similarly, we qualitatively explain the relationship between the normal stress difference at the two boundaries and the motion of the particles in Figures 3.6 and 3.7. However, there are unanswered questions about the distinct evolution of the stress difference and the average velocity after the maximum and about their increase in  $H/H_0 < 0.2$ . So, the evolution of the local microstructure is investigated for the next step.

### 3.3.3 Microstructural development

The contact number ( $N_C$ ) is evaluated for all of the particles located at the interface ( $z = H$ ) and the substrate ( $z = a_L$ ). The contact number is calculated based on the type of contact, i.e., between the large particles ( $N_{C,LL}$ ), between the small particles ( $N_{C,SS}$ ), and between the large and small particles ( $N_{C,LS}$ ). For each type of contact, the number of particles is counted according to each contact number, and this count is divided by the total number of the same species located at position  $z$  ( $z = H$  or  $a_L$ ). As a result, the contact number distribution  $P(z, N_C)$  is given in the form of a probability function and is observed with time. In Figure 3.8, the evolution of the contact number distribution at the substrate,  $P(a_L, N_C)$ , is shown to capture the microstructural change after the accumulation front touches the substrate.

Figure 3.8(a) shows the large–large contact number distribution with the film thickness,  $H/H_0$ . For all  $Pe_L$ , the probability of  $N_{C,LL} = 0$  is significantly higher than that of  $N_{C,LL} \geq 1$  in the beginning of drying, indicating that only a few contacts exist. This distribution is maintained even after  $H/H_0 = 0.7$ . When  $Pe_L = 6$ , the probability of  $N_{C,LL} \geq 1$  starts to increase from  $H/H_0 \sim 0.6$  and shows a continuous increase. As the  $Pe_L$  increases, the contact number increases at a lower film thickness, such as  $H/H_0 \sim 0.5$  for  $Pe_L = 30$  and  $H/H_0 \sim 0.4$  for  $Pe_L = 60$ . This is attributed to the accumulation front touching the substrate at a lower film thickness with increasing  $Pe_L$ . At the final stage of drying, the mean of the contact number distribution is the smallest when  $Pe_L = 6$ .

Figure 3.8(b) shows the small–small contact number distribution with



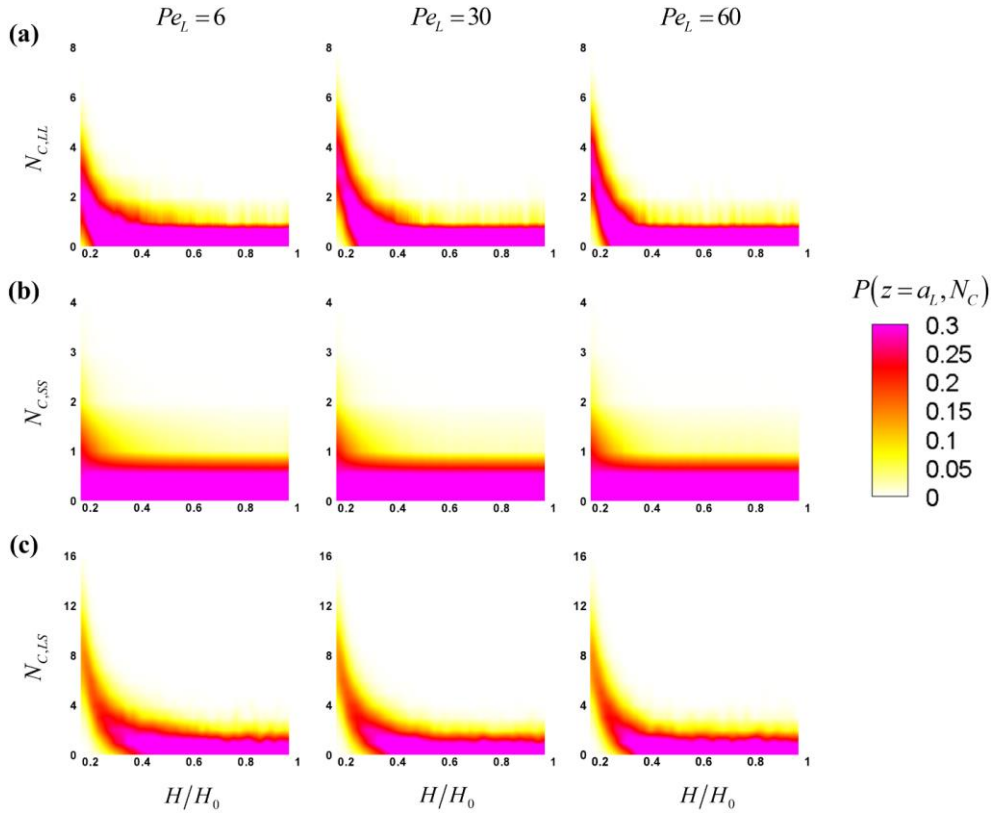


**Figure 3.8** Evolution of the contact number distribution at the substrate  $P(z=a_L, N_C)$ . The contact number is computed for each type of contact: (a) large-large ( $N_{C,LL}$ ); (b) small-small ( $N_{C,SS}$ ); (c) large-small ( $N_{C,LS}$ ) contact.

the film thickness. For all  $Pe_L$ , the small–small contact begins to increase at a lower film thickness than the large–large contact. At the final stage, the distributions are similar in all  $Pe_L$ , and the mean of the distribution is much lower than the mean of the large–large contact. Figure 3.8(c) shows the large–small contact number distribution according to the film thickness. For all  $Pe_L$ , the large–small contact begins to increase at a higher film thickness than the large–large contact. At the final stage, the mean of the distribution is higher compared to the other types of contact and is the highest at  $Pe_L = 6$ .

From the observations of the contact number distribution, we can get an idea of the microstructure on the substrate. The large particles occupy a large volume, resulting in a high contact number between the large particles. Also, the large particles are surrounded by the small particles, resulting in a high large–small contact number. Because the large–small contact cannot occur as much as the contact between the large particles, when the large–large contact number is high, the large–small contact number is relatively low. In addition, the small particles reside in the remaining volume of the large particles, so that many small particles cannot be collected, which leads to a low small–small contact number.

Figure 3.9 shows the contact number distribution at the interface relative to the distribution at the substrate, i.e.,  $P(H, N_c) - P(a_L, N_c)$ . A positive value of the difference means that the probability of the particles with the corresponding  $N_c$  is higher at the interface and a negative value means that such probability is higher at the substrate.

The difference between the two distributions can be useful to analyze the microstructural difference between the interface and substrate. For example, when the difference is positive at high  $N_{C,LL}$ , the probability of large particles with high  $N_{C,LL}$  is higher at the interface than that at the substrate, and in turn, a structure that the large particles are in more contact can be predicted at the interface.

First, in Figure 3.9(a), the large-large contact number distribution is shown with the film thickness. For all  $Pe_L$ , the probability of  $N_{C,LL} = 1$  and 2 is higher at the interface in the initial stage, which is related to a higher probability of  $N_{C,LL} = 0$  at the substrate. When  $Pe_L = 6$ , the probability of high  $N_{C,LL}$  is larger at the interface during the entire drying process. And in  $H/H_0 < 0.6$ , the probability for  $N_{C,LL} \geq 2$  at the interface continuously increases as the film thickness decreases. This is because the large particles approach the interface during drying, and are continuously trapped to form a layer (Figures 3.2, 3.3). When  $Pe_L = 30$ , the probability of high  $N_{C,LL}$  is larger at the interface until  $H/H_0 > 0.4$ , attributed to the accumulation of large particles in the beginning of drying. Also, the depletion of the large particles occurs near the interface so that the contact number at the interface does not increase much. Interestingly, in  $H/H_0 < 0.4$ , a significant increase is observed in the contact number at the substrate. This can be explained that there are many large particles in the accumulation region due to stratification (Figure 3.3), resulting in a rapid increase in the contact number after these large particles reach the substrate. When  $Pe_L = 60$ , the pattern is similar to when  $Pe_L = 30$ , which is related to the small-on-top

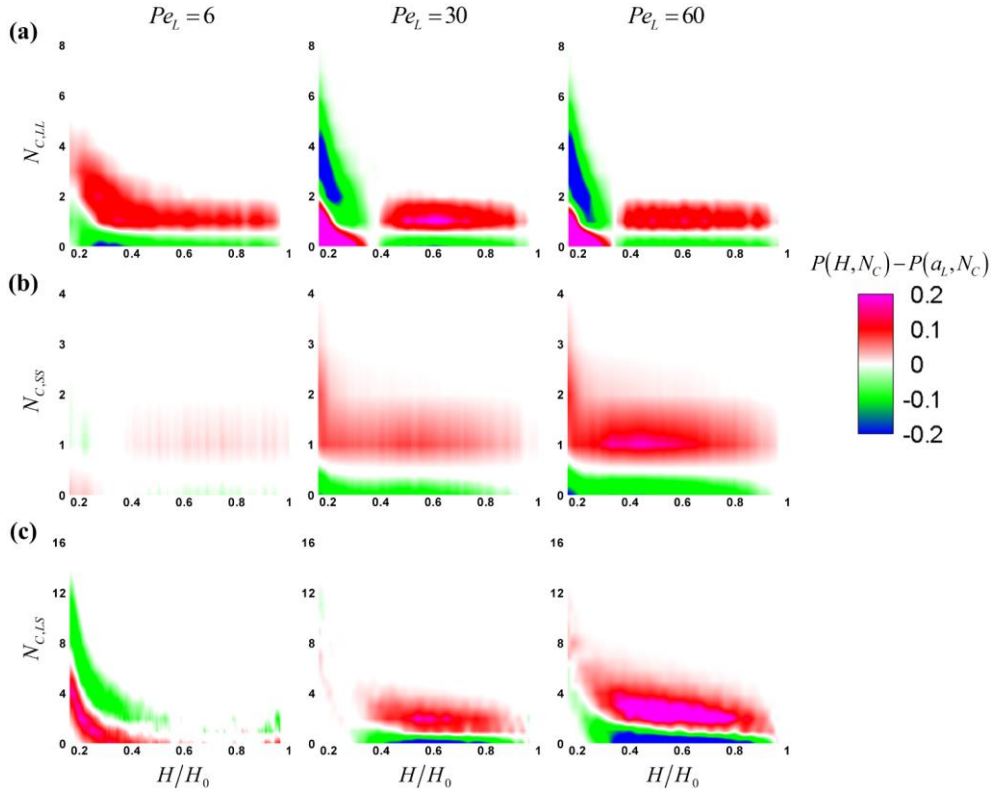


**Figure 3.9** Evolution of the contact number distribution at the interface,  $P(H, N_C)$ , relative to the substrate,  $P(a_L, N_C)$ , i.e.,  $P(H, N_C) - P(a_L, N_C)$ . (a) large-large ( $N_{C,LL}$ ); (b) small-small ( $N_{C,SS}$ ); (c) large-small ( $N_{C,LS}$ ) contact.

stratification.

In Figure 3.9(b), the small–small contact number distribution is shown with the film thickness. When  $Pe_L = 6$ , the difference is very small in the distributions at the interface and substrate. This indicates that the contact between the small particles appears a little at the interface, similar to the substrate. When  $Pe_L = 30$ , the probability of high  $N_{C,SS}$  is larger at the interface from the beginning of drying and increases further as the film thickness decreases. This is due to the accumulation of the small particles at the interface. The probability of high  $N_{C,SS}$  remains higher at the interface even after the accumulation front touches the substrate, i.e.,  $H/H_0 < 0.5$ . Furthermore, we emphasize that in  $H/H_0 < 0.2$ , a sharp increase is observed in the contact number at the interface. In  $H/H_0 < 0.2$ , the bulk particle volume fraction is very high ( $\phi_{\text{bulk}} \geq 0.5$ ) and the average distance between the particles is small. Therefore, this increase can be attributed to the acceleration of the contact between the small particles arising from the compression effect by the descending interface.[71, 72] When  $Pe_L = 60$ , more dominant evaporation intensifies the accumulation of the small particles at the interface, which results in a higher contact number at the interface compared to  $Pe_L = 30$ . In  $H/H_0 < 0.2$ , a sharp increase is also observed at the interface.

In Figure 3.9(c), the large–small contact number distribution is shown with the film thickness. When  $Pe_L = 6$ , the distribution is almost uniform at both the interface and substrate in  $H/H_0 > 0.6$ . In  $H/H_0 < 0.6$ , the contact number increases with time at both, and the probability of high  $N_{C,LS}$  is larger at the substrate than at the interface. This can be related

to the larger probability of high  $N_{C,LL}$  at the interface (Figure 3.9(a)), as discussed earlier (Figure 3.8). When  $Pe_L = 30$ , the probability of high  $N_{C,LS}$  is larger at the interface from the beginning of drying. This is because not only of the accumulation of the small particles but also of the depletion of the large particles. In other words, a few large particles are surrounded by many small particles. However, in  $H/H_0 < 0.4$ , the difference between the two distributions decreases, and as a result, the two distributions become almost uniform at the final stage. When  $Pe_L = 60$ , the probability of high  $N_{C,LS}$  is larger at the interface during the entire drying process. At the interface, the number of small particles is higher and that of large particles is lower compared to  $Pe_L = 30$ , leading to a higher contact number at the interface.

In order to investigate the change of the microstructure related to the contact number distribution, the 2D planar partial pair-distribution function is computed and shown in Figures 3.10 and 3.11 (this analysis is performed at  $H/H_0 = 0.18$ , where all types of contact numbers are sufficiently high.).[85] The partial pair-distribution function is obtained using particle distribution located at the interface ( $z = H$ ) and the substrate ( $z = a_L$ ). Figure 3.10 shows the position of the small particles based on the large particles,  $g_{xy}^{LS}(\mathbf{r}_{xy})$ , and Figure 3.11 shows the position of the small particles based on the small particles,  $g_{xy}^{SS}(\mathbf{r}_{xy})$ . Note that  $g_{xy}^{LL}(\mathbf{r}_{xy})$  is not plotted due to a large noise at the interface at high  $Pe_L$ , which arises from the insufficient number of the large particles.

First, we analyze the results in Figure 3.10. When  $Pe_L = 6$ ,  $g_{xy}^{LS}(\mathbf{r}_{xy})$

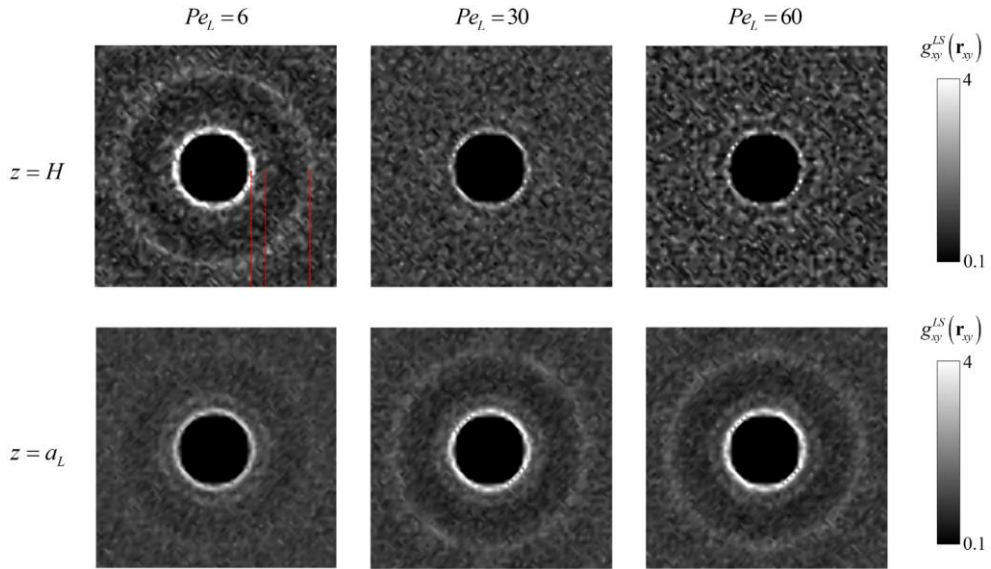


**Figure 3.10** 2D planar partial pair-distribution function for the position of the small particles based on the large particles,  $g_{xy}^{LS}(\mathbf{r}_{xy})$  (at  $H/H_0 = 0.18$ ), at the interface ( $z = H$ ) and substrate ( $z = a_L$ ). Red lines indicate the peaks near  $r_{xy} = a_L + a_s$ ,  $a_L + 3a_s$ , and  $3a_L + a_s$  from the left, respectively.

shows a bright peak near  $r_{xy} = a_L + a_S$  and weak peaks near  $r_{xy} = a_L + 3a_S$  and  $3a_L + a_S$  at the interface. All the peaks are less clear at the substrate than that at the interface. This is due to the higher volume fraction of the large particles at the interface than that at the substrate (Figures 3.2, 3.3), which suggests that the volume fraction of the large particles has a great influence on the formation of a packed structure. In addition, a similar pattern to the interface of  $Pe_L = 6$  appears to the substrate of  $Pe_L = 30$  and  $60$ . At high  $Pe_L$ , the large particles are depleted from the interface and many of them exist near the substrate so that a packed structure can be formed near the substrate. At the interface, two weak peaks near  $r_{xy} = a_L + a_S$ , and  $a_L + 3a_S$  are observed. These two peaks suggest a structure where the large particles are surrounded by many small particles.

In Figure 3.11, when  $Pe_L = 6$ ,  $g_{xy}^{SS}(\mathbf{r}_{xy})$  shows a bright peak near  $r_{xy} = 2a_S$  and weak peaks near  $r_{xy} = 4a_S$  and  $2a_L + 2a_S$  at the interface. Here, a peak near  $r_{xy} = 6a_S$  does not appear, which suggests that the arrangement of the small particles is hindered by the large particles. All the peaks are unclear at the substrate compared to the interface, which suggests that the distribution of the small particles is greatly influenced by the large particles. In addition, a similar pattern to the interface of  $Pe_L = 6$  is also observed at the substrate of higher  $Pe_L$ . Interestingly, although the small particles are accumulated at the interface at higher  $Pe_L$  (Figure 3.3), the peaks near  $r_{xy} = 2a_S$  and  $4a_S$  are brighter at the substrate than that at the interface. This result also supports that the large particles significantly



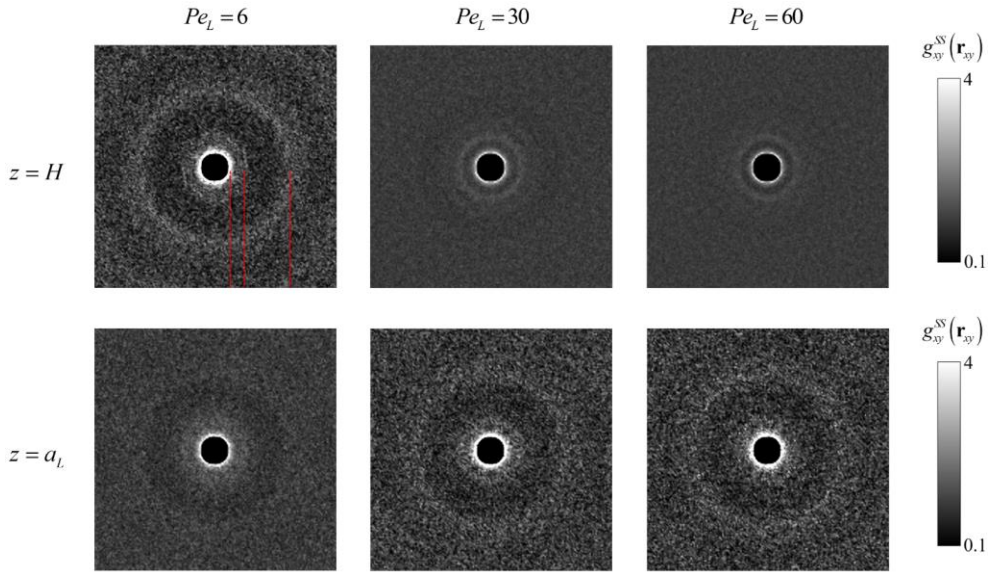


**Figure 3.11** 2D planar partial pair-distribution function for the position of the small particles based on the small particles,  $g_{xy}^{SS}(\mathbf{r}_{xy})$  (at  $H/H_0 = 0.18$ ), at the interface ( $z = H$ ) and substrate ( $z = a_L$ ). Red lines indicate the peaks near  $r_{xy} = 2a_S$ ,  $4a_S$ , and  $2a_L + 2a_S$  from the left, respectively.

affect the distribution of the small particles.

To sum up, the evolution of the normal stress difference (Figure 3.6) and the contact number distribution (Figures 3.8, 3.9) can be correlated as follows. When  $Pe_L = 6$ , the increasing normal stress difference from the beginning of drying becomes constant after the accumulation front reaches the substrate, i.e.,  $H/H_0 < 0.7$ . In  $0.6 < H/H_0 < 0.7$ , the volume fraction of the two types of particles increases at both the interface and substrate, but the contact number distribution is almost consistent at both, resulting in the constant normal stress difference. In  $H/H_0 < 0.6$ , the increase in the large-large contact at the interface is counterbalanced by the increase in the large-small contact at the substrate, leading to the constant normal stress difference. For higher  $Pe_L$ , the large-large and large-small contact start to increase at the substrate with the accumulation front touching the substrate. The increasing volume fraction and contact number induce the acceleration of the normal stress development at the substrate, and therefore, the normal stress difference decreases as the film thickness decreases.

Furthermore, the increase in the normal stress difference in  $H/H_0 < 0.2$  can be explained by the correlation of the contact number distribution and partial pair-distribution function (Figures 3.10, 3.11). When  $Pe_L = 6$ , the packed structure is formed at low film thickness. A continuing descent of the interface gives rise to the compression of this packed structure, which results in the localization of the stress at the interface. For higher  $Pe_L$ , the small particles are accumulated at the interface, and the contact between the small particles sharply increases at the final

stage of drying. A continuing descent of the interface contributes to an increase in the contact between the small particles as well as the arrangement of the small particles, resulting in the localization of the stress at the interface.

Our results of the microstructural analysis can explain the binary crystal structures observed in the experimental studies on the drying process of bi-disperse colloidal film.[20–22, 25, 27] Several studies confirmed that the evaporation-driven binary colloidal crystals (bCCs) were formed at the top surface of the final dried film. In the crystalline domain, the large particles were assembled into a hexagonal close-packed array, and the small particles were located in the interstitial void of the large particles. In this study, at the interface of  $Pe_L = 6$ , the large particles occupy a large volume and contact each other, and the small particles are located in the remaining volume of the large particles, which is connected to the bCCs. On the other hand, at  $Pe_L = 60$ , the stratified layer prevents the large particles from accessing the interface so that the volume fraction of the large particles remains constant. Accordingly, a close-packed array of the large particles does not appear at the interface, which suggests that the bCCs cannot be formed.

### 3.4 Summary

In this chapter, the evolution of the normal stress and microstructure in the drying process of bi-disperse colloidal film has been studied by using the Brownian dynamics simulation. Simulations are carried out over a wide range of Peclet numbers ( $Pe_L$ ) to investigate the formation process of the small-on-top stratification in colloidal mixtures of two different sizes. At low  $Pe_L$  ( $Pe_L = 6$ ), the stratification does not occur, and the layer dominated by the large particles is formed at the interface. At high  $Pe_L$  ( $Pe_L = 30, 60$ ), the large particles are depleted from the interface, and the stratified layer of small particles is formed near the interface. In all  $Pe_L$  we have tested, the particles are accumulated near the interface due to evaporation dominance ( $Pe_L > 1$ ), and accumulated particles result in the localization of the normal stress so that the normal stress at the interface increases from the beginning of drying. At the substrate, the normal stress maintains its initial value and then increases with the accumulation region touching the substrate.

The localization of the normal stress is quantified by the scaled normal stress difference between the interface and substrate. In all  $Pe_L$ , the scaled normal stress difference increases with decreasing film thickness until the accumulation region contacts the substrate. As  $Pe_L$  increases, the thickness of the accumulation region decreases at the same film thickness, which leads to the lower scaled normal stress difference at the initial stage of drying. The stress difference shows the distinct evolution after the maximum. At low  $Pe_L$ , the stress difference remains at the maximum, however, at high  $Pe_L$ , it decreases. The reasons for this

stress development are explained by the evolution of the contact number distribution at the two boundaries. At low  $Pe_L$ , the large–large contact number is higher at the interface, but the large–small contact number is higher at the substrate. As a result, two effects balance each other, resulting in the constant stress difference after the maximum. At high  $Pe_L$ , the large–large and large–small contact number are higher at the substrate due to the higher volume fraction of the large particles. As a result, the normal stress development is accelerated at the substrate, leading to a decrease in the stress difference.

Interestingly, for all  $Pe_L$ , the scaled normal stress difference increases again at low film thickness ( $H/H_0 < 0.2$ ). This is also explained by the contact number distribution. At low  $Pe_L$ , a continuing descent of the interface gives rise to the compression of the particle structure, which can result in the localization of the stress at the interface. At high  $Pe_L$ , a continuing descent of the interface leads to a sharp increase in the contact between the small particles as well as the arrangement of the small particles, resulting in the localization of the stress at the interface.

## Chapter 4.

### Stratification mechanism on the local length scale

## 4.1 Introduction

It was not sufficiently explained in the previous Chapter 3. why the large particles preferentially move toward the substrate compared to the small particles. In this chapter, we investigate the force acting on each species on the particle length scale to understand the different behavior of the two species. The local forces applied to each species are derived by a decomposition of the local normal stress. The development of the local force field is analyzed in detail to present the process of stratification. In addition, the local microstructural development is closely investigated to interrogate the local force response. As a result, the physical origin of the stratification is explained in terms of the local normal stress.

## 4.2 Derivation of the local force field

In order to analyze the effect of the local normal stress on different species, the normal stress from the inter-particle forces is decomposed according to the type of interacting particles. The expression is as follows

$$\langle \Sigma_{zz}(z) \rangle = -\langle n_L(z) \rangle k_B T - \langle n_S(z) \rangle k_B T + \langle \Sigma_{zz}^{P,LL}(z) \rangle + \langle \Sigma_{zz}^{P,SS}(z) \rangle + \langle \Sigma_{zz}^{P,LS}(z) \rangle. \quad (4.1)$$

The last three terms on the right-hand side are corresponding to the interaction of large-large, small-small, and large-small particles, respectively. Based on the above equation, we derive the local forces acting on the different species, which is originated from the local normal stress gradient.

We assume that only the motion in the  $z$ -direction is relevant in the drying process, i.e. one-dimensional system. In this case, the gradient in the  $zz$ -component of the normal stress is equal to the force per unit volume in the  $z$ -direction. [67, 68] The microscopic expression is

$$\partial \langle \Sigma_{zz}(z) \rangle / \partial z = \sum_{i=1}^{N_L} \langle \delta(z - z_i) f_{iz}^L \rangle + \sum_{j=1}^{N_S} \langle \delta(z - z_j) f_{jz}^S \rangle = F_z^L(z) + F_z^S(z) \quad (4.2)$$

where  $f_{iz}^L$  is the net force in the  $z$ -direction exerted on the  $i^{\text{th}}$  large particle due to the interaction between the particles. The force includes the contributions from the Brownian motion, the interaction between the large particles, and between the large and small particles.  $f_{jz}^S$  is the net force in the  $z$ -direction exerted on the  $j^{\text{th}}$  small particle due to the interaction between the particles. Similarly, the force includes the



contributions from the Brownian motion, the interaction between the small particles, and between the small and large particles.  $F_z^m(z)$  is the local force density in the  $z$ -direction exerted on the type  $m$  particle ( $m = L, S$ ). In eqn (4.2), the local force density for each type of particle can be derived from the decomposition of the normal stress by its components in eqn (4.1). In the components, the Brownian stress of the type  $m$  particle and the normal stress from the inter-particle forces between the type  $m$  particles induce the net motion of the type  $m$  particle to reduce the gradient. Accordingly, these two stress terms can be represented by another stress term. Eqns (4.1) and (4.2) give

$$\langle \Sigma_{zz}(z) \rangle = \langle \Sigma_{zz}^L(z) \rangle + \langle \Sigma_{zz}^S(z) \rangle + \langle \Sigma_{zz}^{LS}(z) \rangle \quad (4.3)$$

$$\langle \Sigma_{zz}^{mm}(z) \rangle = -\langle n_m(z) \rangle k_B T + \langle \Sigma_{zz}^{P,mm}(z) \rangle \quad (4.4)$$

$$F_z^{mm}(z) = \partial \langle \Sigma_{zz}^{mm}(z) \rangle / \partial z, \quad m = L, S \quad (4.5)$$

The normal stress from the interaction between the different species gives rise to the net motion of the particle in another mechanism. For example, when the center of a large particle is above or below the center of a small particle at the collision, the upward or downward motion for the large particle is created, respectively. Therefore, this stress term can be decomposed into

$$\langle \Sigma_{zz}^{P,LS}(z) \rangle = \langle \Sigma_{zz-}^{P,LS}(z) \rangle + \langle \Sigma_{zz+}^{P,LS}(z) \rangle = \langle \Sigma_{zz-}^{P,SL}(z) \rangle + \langle \Sigma_{zz+}^{P,SL}(z) \rangle \quad (4.6)$$

where  $\Sigma_{zz-}^{P,mm}$  and  $\Sigma_{zz+}^{P,mm}$  represent that in the normal stress due to the interaction between the type  $m$  and  $n$  particles, a normal stress

component to move the type  $m$  particle in the  $-z$  and  $+z$  direction, respectively. When the volume fraction of the small particles relative to that of the large particles is almost consistent in the  $z$ -direction,  $\Sigma_{zz,-}^{P,LS}$  is almost equal to  $\Sigma_{zz,+}^{P,LS}$ , which cannot induce the net motion of the particle. On the other hand, when it increases in the  $+z$  direction,  $\Sigma_{zz,-}^{P,LS}$  becomes larger than  $\Sigma_{zz,+}^{P,LS}$ , which induces the net motion of the large particle to  $-z$  direction (of the small particle to  $+z$  direction).

The gradient of  $\Sigma_{zz}^{P,LS}$  is also the force per unit volume in the  $z$ -direction.

$$\partial \langle \Sigma_{zz}^{P,LS}(z) \rangle / \partial z = \sum_{i=1}^{N_L} \langle \delta(z - z_i) f_{iz}^{LS} \rangle + \sum_{j=1}^{N_S} \langle \delta(z - z_j) f_{jz}^{SL} \rangle = F_z^{LS}(z) + F_z^{SL}(z) \quad (4.7)$$

where  $f_{iz}^{mn}$  is the force in the  $z$ -direction exerted on the  $i^{\text{th}}$  type  $m$  particle due to the type  $n$  particles.  $F_z^{mn}$  is the local force density in the  $z$ -direction exerted on the type  $m$  particle due to the type  $n$  particles. Furthermore, considering the decomposed stress terms in eqn (4.6), the gradient of  $\Sigma_{zz}^{P,LS}$  can be written by

$$\partial \langle \Sigma_{zz}^{P,LS}(z) \rangle / \partial z = \partial \left\{ \langle \Sigma_{zz}^P(z) \rangle + \langle \Sigma_{zz}^{P,LS}(z) \rangle \right\} / \partial z. \quad (4.8)$$

Here, the right-hand side of eqn (4.8) can be rewritten by introducing an infinitesimal height  $\delta z$ , which gives

$$\lim_{\delta z \rightarrow 0} \left\{ \langle \Sigma_{zz}^{P,LS}(z + \delta z) \rangle + \langle \Sigma_{zz}^P(z + \delta z) \rangle - \langle \Sigma_{zz}^{P,LS}(z) \rangle - \langle \Sigma_{zz}^P(z) \rangle \right\} / \delta z. \quad (4.9)$$

Because of  $\Sigma_{zz,-}^{P,mn} = \Sigma_{zz,+}^{P,mn}$ , eqn (4.9) can be reorganized,

$$\lim_{\delta_z \rightarrow 0} \left\{ \langle \Sigma_{zz^-}^{P,LS}(z + \delta_z) \rangle - \langle \Sigma_{zz^+}^{P,LS}(z) \rangle + \langle \Sigma_{zz^-}^{P,SL}(z + \delta_z) \rangle - \langle \Sigma_{zz^+}^{P,SL}(z) \rangle \right\} / \delta_z. \quad (4.10)$$

From the eqns (4.7)–(4.10), the local force density due to the interaction between the type  $m$  and  $n$  particles is

$$\lim_{\delta_z \rightarrow 0} \left\{ \langle \Sigma_{zz^-}^{P,mm}(z + \delta_z) \rangle - \langle \Sigma_{zz^+}^{P,mm}(z) \rangle \right\} / \delta_z = F_z^{mm}(z). \quad (4.11)$$

Hence, from the eqns (4.2)–(4.11), the local force density for each type of particle is expressed as

$$F_z^L(z) = F_z^{LL}(z) + F_z^{LS}(z), \quad F_z^S(z) = F_z^{SS}(z) + F_z^{SL}(z) \quad (4.12)$$

The net force exerted on the particle is the integration of the local force density over the volume of the particle [67, 68]

$$f_z^m(z) = \int_{V_m} F_z^m(z) dV \quad (4.13)$$

where  $V_m$  is the volume of a type  $m$  ( $m = L, S$ ) particle. The local net force in the  $z$ -direction on the type  $m$  particle,  $f_z^m(z)$ , is computed by integrating the local force density over the volume of the type  $m$  particle, assuming that the center of the particle is located at that position  $z$ .

## 4.3 Results and discussion

### 4.3.1 Evolution of local force field

The net force can be decomposed according to the types of interaction. For the large particle, the net force is composed of the force from the interaction between the large particles,  $f_z^{LL}(z)$ , and the one from the interaction with the small particles,  $f_z^{LS}(z)$ . For the small particle, the net force is composed of the force from the interaction between the small particles,  $f_z^{SS}(z)$ , and the one from the interaction with the large particles,  $f_z^{SL}(z)$ .

Figure 4.1 shows the evolution of the local force field for each type of particle at  $Pe_L = 60$ . The local force field is plotted from the substrate ( $z = a_L$ ) to the interface ( $z = H$ ) as a function of the film thickness,  $H/H_0$ . The local force is scaled by  $\zeta_m \dot{E}$ ,  $m = L, S$ , which is the force to move the particle at the evaporation rate. Here, a  $(-)$  sign is used to convert the force in the  $-z$  direction into a  $(+)$  sign (because the evaporation rate is expressed as a  $(+)$  sign). By the definition, the  $(+)$  or  $(-)$  sign of the scaled force indicates that the net force acts on the particle in the direction of the substrate or interface, respectively.

For the large particle (Figures 4.1(a), (b)),  $f_z^{LL}(z)$  (Figure 4.1(a)) shows a negative scaled force near the interface (i.e.,  $0.29 < z/H_0 < 0.33$  at  $H/H_0 = 0.4$ ) and positive scaled force beneath that negative ( $0.14 < z/H_0 < 0.24$ ). These negative and positive scaled forces become stronger as the film thickness decreases.  $f_z^{LS}(z)$  (Figure 4.1(b)) shows a negative scaled force at the interface, and a positive scaled force

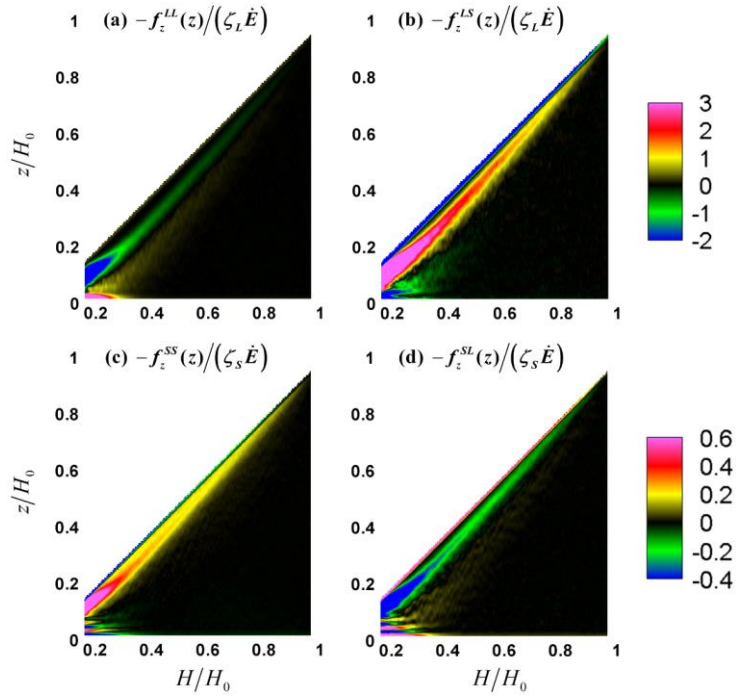


**Figure 4.1** Evolution of the scaled local force field during drying at  $Pe_L = 60$ . The local force from the substrate ( $z = a_L$ ) to the interface ( $z = H$ ) is shown at the corresponding film thickness. The local force is computed according to the types of interacting particles. (a)  $f_z^{LL}(z)$ ; (b)  $f_z^{LS}(z)$ ; (c)  $f_z^{SS}(z)$ ; (d)  $f_z^{SL}(z)$ . A  $(-)$  sign is used to convert the force in the  $-z$  direction into a  $(+)$  sign.

beneath that negative. Interestingly, the positive scaled force becomes stronger and larger than 1.0 with decreasing film thickness. This suggests that the large particles are strongly forced to the substrate by the small particles and are pushed faster than the evaporation rate, which leads to the stratified layer of only small particles.

For the small particle (Figures 4.1(c), (d)),  $f_z^{SS}(z)$  (Figure 4.1(c)) shows a positive scaled force near the interface and this force becomes stronger with decreasing film thickness.  $f_z^{SL}(z)$  (Figure 4.1(d)) shows a negative scaled force near the interface, which becomes stronger with decreasing film thickness. This negative force can be correlated with the positive scaled force in  $f_z^{LS}(z)$ . The small particles pushing the large particles toward the substrate receive the reaction force toward the interface.

The scaled local force field (Figure 4.1) can be qualitatively explained with the local volume fraction profile (Figure 3.3). The negative and positive scaled forces in  $f_z^{LL}(z)$  are observed in the upper part of the accumulation region. The volume fraction of the large particles is the highest in a region between the two scaled forces, which pushes the large particles to move to both the upper (negative scaled force) and lower (positive scaled force) regions to reduce the volume fraction gradient. In addition, the volume fraction of the small particles is the highest at the interface and continuously increases during drying, which results in the positive scaled force in  $f_z^{SS}(z)$  and  $f_z^{LS}(z)$ .

Note that in both Figures 4.1(c) and (d), the intercalated zone where

the positive and negative scaled forces appear alternately is formed near the substrate in  $H/H_0 \leq 0.4$  (the intercalated zone is zoomed in and presented in Figure 4.2(a)). This can be explained by the particle structure. In Figure 4.2(b), the particle configuration near the substrate is shown at  $H/H_0 = 0.18$ . *Zone 1* and 2 represent the first and second layers of the large particles from the substrate, respectively. In each *zone*, when the center of the small particle is below or above the center of the layer of large particles, a positive or negative scaled force is exerted to the small particle from the large particle, respectively. Furthermore, in each *zone*, the direction of  $f_z^{SS}(z)$  is toward the center of the *zone*, which is due to the volume fraction gradient of the small particles. Thus, the signal of the alternating sign may indicate the structure in which the small particles reside in the arrangement of the large particles. Indeed, this signal begins to be formed at the film thickness  $H/H_0 \sim 0.4$  where the accumulation front begins to touch the substrate and grows upward as the film thickness decreases.

Figure 4.3 shows the evolution of the scaled local net force field in the  $z$ -direction for each type of particle. The local net force is the sum of the local forces according to the types of interacting particles:  $f_z^L(z) = f_z^{LL}(z) + f_z^{LS}(z)$ ,  $f_z^S(z) = f_z^{SS}(z) + f_z^{SL}(z)$ .

When  $Pe_L = 6$  (Figure 4.3), in  $H/H_0 > 0.6$ , the scaled force is almost 0 inside the film, and a signal appears only at the interface for both large and small particles. At the interface, a negative scaled force is observed for the large particle arising from the interaction with the small particles (Figure 4.1(b)). The large particles located at the interface descend

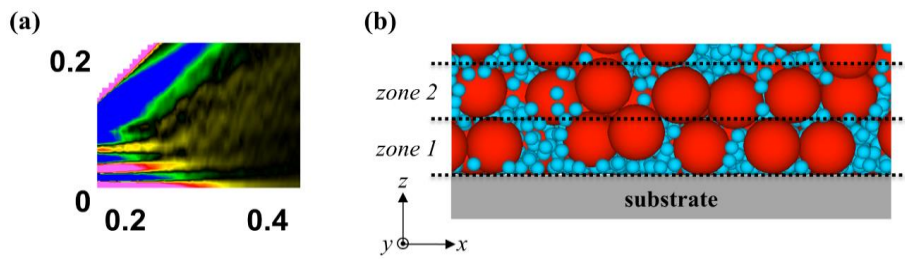


**Figure 4.2** (a) Zoom-in on the intercalated zone in the scaled local force field of small-large interaction,  $f_z^{SL}(z)$  for  $H/H_0 \leq 0.4$ . (b) Snapshot of the particle configuration near the substrate at  $H/H_0 = 0.18$  for  $Pe_L = 60$ .



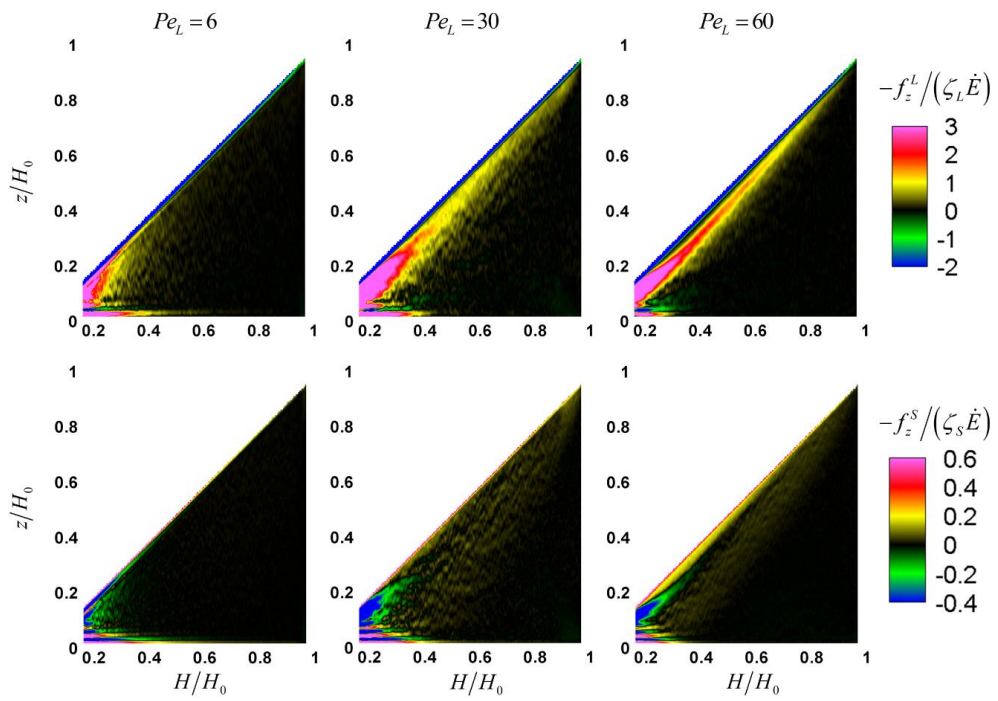


**Figure 4.3** The evolution of the scaled local net force field during drying. The local net force is the sum of the local forces according to the types of interaction.

along with the interface and push the small particles below downward, resulting in a positive scaled force for the small particle at the interface. In  $H/H_0 < 0.6$ , for the large particle, a positive scaled force becomes stronger near the two boundaries as the film thickness decreases, and at the final stage, the positive scaled force is observed in most of the film. For the small particle, the intercalated zone grows from the substrate (Figures 4.1(c), (d)). Furthermore, this zone also grows from the interface in  $H/H_0 < 0.5$ . At the final stage, the intercalated zone is observed in the entire film, which suggests that the large particles are arranged in the entire film, and the small particles reside between the large particles and interact with them.

At high  $Pe_L$  ( $= 30, 60$ ), a positive scaled force is observed near the interface for the large and small particles from the initial stage. This scaled force is stronger and thinner for  $Pe_L = 60$  compared to that for  $Pe_L = 30$ . The positive scaled force for the large particle arises from the interaction with the small particles and for the small particle from the interaction between the small particles (Figures 4.1(b), (c)). Interestingly, for the large particle, the scaled force is initially close to 1 and becomes higher with decreasing film thickness. For the small particle, however, the scaled force shows a value lower than 0.2 during the drying process. Accordingly, the depletion of the large particles occurs near the interface due to the difference in the descending rate of the two species. At the final stage, the positive scaled force is observed in most of the film for the large particle. On the other hand, for the small particle, the intercalated zone is observed near the substrate, but a

negative scaled force is predominant near the interface. This can be related to the packed structure formed near the substrate (Figure 4.2). The small particles in the packed structure show the signal of the alternating sign, and the small particles above the packed structure are forced upward by the structure, which shows the negative scaled force.

### 4.3.2 Local force field and local volume fraction profile

In Figures 4.1 and 4.3, the large particles experience a strong force to the substrate direction at high  $Pe_L$  due to the small particles accumulated near the interface. This force is developed from the beginning of drying and increases as drying progresses. Therefore, to explain the origin of the force, we carefully analyze the developing force in the early stage of drying. For this purpose, the scaled local force field at  $H/H_0 = 0.9$  when  $Pe_L = 60$  is shown in Figure 4.4(a). In addition, to demonstrate the correlation between the local force and particle distribution, the local volume fraction profile at  $H/H_0 = 0.9$  when  $Pe_L = 60$  is shown in Figure 4.4(b).

Figure 4.4(a) represents the scaled local force field near the interface ( $z/H_0 \geq 0.75$ ). At the interface ( $z/H_0 = 0.90$ ),  $f_z^{LL}(z)$  and  $f_z^{SL}(z)$  show a positive scaled force, while  $f_z^{LS}(z)$  and  $f_z^{SS}(z)$  show a negative scaled force. The negative value of  $f_z^{LS}(z)$  is about 18 times larger than the positive value of  $f_z^{LL}(z)$ , which suggests that this force field plays a critical role in trapping the large particles at the interface (see Figure 3.3). Below the interface, in  $z/H_0 < 0.88$ , all types of scaled forces have opposite signs to the interface. The maximum value of  $f_z^{LS}(z)$  is more than 5 times larger than those of the other scaled forces. This force field can induce the large particles to preferentially move away from the interface compared to the small particles. Moreover, all types of scaled forces approach 0 with decreasing position  $z$ .

Figure 4.4(b) represents the local volume fraction profile near the

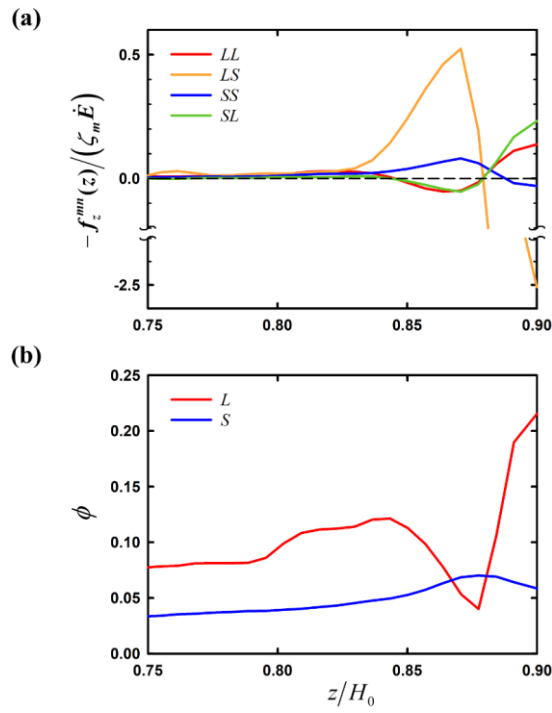


**Figure 4.4.** (a) Scaled local force field near the interface at  $H/H_0 = 0.9$  for  $Pe_L = 60$ . (b) Local volume fraction profile near the interface at  $H/H_0 = 0.9$  for  $Pe_L = 60$ .

interface at  $H/H_0 = 0.9$  ( $Pe_L = 60$ ). For the large particle, the volume fraction shows the maximum at the interface, and the minimum is observed at  $z/H_0 \sim 0.88$ . In  $0.84 < z/H_0 < 0.88$ , the volume fraction increases with decreasing position  $z$ , and it decreases again in  $z/H_0 < 0.84$ . For the small particles, the volume fraction shows the maximum at  $z/H_0 \sim 0.88$ , and it decreases with decreasing position  $z$ . Due to the scaled force  $f_z^{LS}(z)$ , the large particles approaching the interface are trapped, and those located in  $z/H_0 < 0.88$  are pushed to the substrate direction so that the minimum of  $\phi_L$  appears at  $z/H_0 \sim 0.88$ . On the other hand, the maximum of  $\phi_S$  appears at  $z/H_0 \sim 0.88$  due to the scaled force  $f_z^{SL}(z)$ . Interestingly, the position  $z$  where the sign of  $f_z^{LS}(z)$  and  $f_z^{SL}(z)$  changes is almost equal to the position  $z$  where the minimum of  $\phi_L$  and the maximum of  $\phi_S$  appear. Through these observations, we can suggest that the sign of the scaled local force is closely related to the gradient of the local volume fraction. More specifically,  $f_z^{LL}(z)$  and  $f_z^{SS}(z)$  can act on each type of particle down the volume fraction gradient of  $\phi_L$  and  $\phi_S$ , respectively. This is due not only to particle diffusion but also to the contact between the same species. At a high volume fraction, the average distance between the particles is small and the particles frequently contact each other, which gives rise to the repulsive force in the direction where the volume fraction decreases. At the interface, the volume fraction decreases for the large particle and increases for the small particle with decreasing  $z/H_0$ . Thus, the forces push the particles in the  $-z$  direction for the large and in the  $+z$  direction for the small

particle, which is in agreement with the positive scaled force of  $f_z^{LL}(z)$  and the negative scaled force of  $f_z^{SS}(z)$ . Furthermore, the average number of small particles in contact with large ones increases significantly with decreasing  $z/H_0$  due to a decrease of  $\phi_L$  and an increase of  $\phi_s$ . These contacts push the large particles in the  $+z$  direction, which is associated with the negative scaled force of  $f_z^{LS}(z)$ . Likewise, the average number of large particles in contact with small ones decreases with decreasing  $z/H_0$  and it is related to the positive scaled force of  $f_z^{SL}(z)$ .

The scaled local force field below the interface can also be explained with the volume fraction gradient (Figure 4.4). In  $0.84 < z/H_0 < 0.88$ , the negative scaled force of  $f_z^{LL}(z)$  and the positive scaled force of  $f_z^{SS}(z)$  can be related to an increase of  $\phi_L$  and a decrease of  $\phi_s$  as  $z/H_0$  decreases. The positive scaled force of  $f_z^{LS}(z)$  and the negative scaled force of  $f_z^{SL}(z)$  are also related to a decrease in the average number of small particles in contact with large ones as  $z/H_0$  decreases. In addition, in  $z/H_0 < 0.84$ , the volume fraction of both particles gradually changes according to the position  $z$ . This can be understood that the interaction between the particles changes slightly according to the position  $z$  so that all types of scaled forces become close to 0.

The correlation of scaled local force and local volume fraction in Figure 4.4 demonstrates that the strong downward force experienced by the large particles arises from the particle distribution in the early stage of drying. The large particles approaching the interface are trapped due

to the interaction with surrounding small particles, and the volume fraction below the interface decreases. On the other hand, the volume fraction of small particles increases below the interface because not only of the accumulation but also of the downward force exerted by the large particles located at the interface. As a result, below the interface, the average number of small particles in contact with large ones increases significantly, which creates a strong force that pushes the large particles toward the substrate.

In Figure 4.4, we suggest that the dominant  $f_z^{LS}(z)$  below the interface is closely related to the distribution of particles. To test this hypothesis, Figure 4.5 represents the development of  $f_z^{LS}(z)$  and the change of volume fraction profile during the drying process for each  $Pe_L$ . The profile is plotted according to the  $z - H$  to set the position  $z$  of the interface to 0 at each film thickness. In addition, the profile is plotted for  $z/H_0 \geq H/H_0 - 0.2$  to focus on the change near the interface.

At the initial stage of drying  $H/H_0 = 0.9$ , below the interface,  $f_z^{LS}(z)$  shows a value close to 0 for  $Pe_L = 6$ , while a positive scaled force for higher  $Pe_L$ . For the volume fraction profile, at all  $Pe_L$ ,  $\phi_L$  is the highest at the interface, followed by the minimum below the interface. This indicates that the large particles are trapped at the interface at the early stage of drying for all  $Pe_L$  we test. In addition,  $\phi_s$  increases near the interface with increasing  $Pe_L$ . From this observation, the formation of  $f_z^{LS}(z)$  can be explained with the volume fraction profile at the beginning of drying. At high  $Pe_L$ , the positive scaled force of  $f_z^{LS}(z)$  is developed



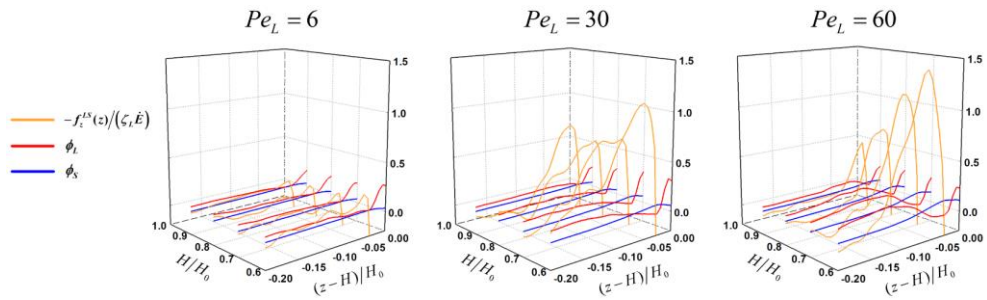


**Figure 4.5** Evolution of the scaled local force field of large–small interaction,  $f_z^{LS}(z)$ , and of the local volume fraction profile near the interface. The profile near the interface,  $(z-H)/H_0 \geq -0.20$ , is shown at the corresponding film thickness.

due to both the low volume fraction of large particles and the high volume fraction of small particles near the interface.

During the drying process,  $f_z^{LS}(z)$  remains at a low value for  $Pe_L = 6$ , which is related to the gradual change in the volume fraction of large and small particles according to the position  $z$ . When  $Pe_L = 30$ ,  $f_z^{LS}(z)$  maintains its maximum value until  $H/H_0 = 0.7$  and increases thereafter. When  $Pe_L = 60$ , the maximum value of  $f_z^{LS}(z)$  continuously increases. In both  $Pe_L = 30$  and  $60$ , as drying proceeds, the minimum value of  $\phi_L$  decreases, and the maximum value of  $\phi_S$  increases below the interface. This result can be understood that the large particles are depleted from the interface due to  $f_z^{LS}(z)$ , while the small particles are continuously accumulated near the interface, which, in turn, gives rise to an increase of  $f_z^{LS}(z)$  as drying proceeds.

To sum up, the mechanism of small-on-top stratification at high  $Pe_L$  can be summarized as follows. Due to the dominant evaporation compared to particle diffusion, both types of particles are accumulated near the interface at the initial stage of drying. The large particles approaching the interface are trapped by the surrounding small particles, and the volume fraction below the interface decreases. On the other hand, the small particles are pushed down by the large particles located at the interface and the volume fraction below the interface increases. As a result, below the interface, the average number of small particles interacting with the large ones increases significantly, which induces a strong force in the substrate direction on the large particles. The

difference in the volume fraction of large and small particles increases as drying proceeds, which results in an increase of this force. Thus, the large particles are depleted near the interface, forming a small-on-top structure.

Our scaled force analysis shares similarities to the force model studied by Fortini *et al.*[26] They modeled the force ( $f$ ) in the thickness ( $z$ ) direction received by the particle with the diameter ( $d$ ) under the osmotic pressure gradient ( $\partial P/\partial z$ ) as  $f(d) \approx d^3(-\partial P/\partial z)$ . This is similar to our scaled force in that the force acting on the particle is obtained by integrating the normal stress gradient over the particle volume. However, there are important differences. We decompose the normal stress by considering the types of interacting particles and derive the scaled force with four components. The force derived from the total normal stress without decomposition can lead to an incorrect prediction of the stratification. For example, the force acts on both types of particles in the substrate direction at all positions in the film because the total normal stress continuously increases from the substrate to the interface (Figure 3.5). In addition, the force on the large particle compared to the small one is proportional to the cube of the size ratio. By these results, the depletion of the large particles can be overestimated. By observing the four components of the scaled force, we confirm that the  $LS$  component of the scaled force significantly contributes to the depletion of large particles near the interface. In addition, we demonstrate that the trapping of the large particles at the interface is induced by the  $LS$  component of the scaled force.[49] Thus, our scaled force analysis is

more accurate to explain the mechanism of small-on-top stratification, compared to the force model proposed by Fortini *et al.*

## 4.4 Summary

In this chapter, the scaled local force applied to each type of particle is derived by a decomposition of the local normal stress. The local force field is computed for both large and small particles to explain the different behaviors of the two types of particles. At high  $Pe_L$ , the scaled force for the large particle is larger than 1 near the interface, indicating that the large particles outrun the descending interface. However, for the small particle, the scaled force near the interface is lower than 1 during the drying process. Therefore, the large particles are depleted from the interface and the small particles are accumulated at the interface, which results in the small-on-top structure. Associating the volume fraction profile with the scaled local force field, we suggest that the strong scaled force for the large particle is attributed to the significant increase of the average number of small particles in contact with the large ones.

Chapter 5.

Concluding remark

In this thesis, the evolution of the normal stress and microstructure in the drying process of colloidal film has been studied by using the Brownian dynamics simulation. The heterogeneous structures formed in the drying of mono- and bi-disperse colloidal films are investigated.

In Chapter 2, the drying mechanism of monodisperse colloidal film is analyzed according to  $Pe$ . When  $Pe > 1$ , the particles are accumulated at the evaporating interface and the accumulation region grows. These accumulated particles localize the normal stress at the interface, which induces the continuous increase of the normal stress from the beginning of the drying process. At the substrate, the normal stress first maintains the initial value and then increases with the accumulation front touching the substrate. The influence of the interface and substrate on stress development has been quantified by the scaled normal stress difference between the two boundaries. At all  $Pe$  discussed in this study ( $Pe = 6 - 60$ ), the scaled normal stress difference increases to the maximum, followed by the decrease in the final stage. As the  $Pe$  decreases, more particles are affected by the interface at the same film thickness so that the initial scaled normal stress difference is higher. Interestingly, a mismatch is observed between the stress difference maximum and the initial stress increase at the substrate. This mismatch is explained by the contact number distribution of the particles. At the substrate, the contact number distribution remains unchanged even though the accumulation front reaches the substrate, and then increases as the particle volume fraction further increases. The increase of contact between the particles results in a significant increase of the normal

stress, which leads to the decrease in the scaled normal stress difference. In addition, the formation of the accumulation region influences the final structure of the film. As the accumulation front contacts the substrate at low film thickness, the disordered structure is formed due to the limited time for particle rearrangement. So, the structure formation at the substrate is more sensitive to  $Pe$  than that at the interface.

In Chapter 3, the drying mechanism of bi-disperse colloidal film is investigated according to  $Pe_L$ . At low  $Pe_L$ , the stratification does not occur, and the layer dominated by the large particles is formed at the interface. At high  $Pe_L$ , the large particles are depleted from the interface, and the stratified layer of small particles is formed near the interface. In all  $Pe_L$  tested in this study, the particles are accumulated near the interface due to evaporation dominance ( $Pe_L > 1$ ), and accumulated particles result in the localization of the normal stress so that the normal stress at the interface increases from the beginning of drying. At the substrate, the normal stress maintains its initial value and then increases with the accumulation region touching the substrate. The localization of the normal stress is quantified by the scaled normal stress difference between the interface and substrate. In all  $Pe_L$ , the scaled normal stress difference increases with decreasing film thickness until the accumulation region contacts the substrate. As the  $Pe_L$  increases, the thickness of the accumulation region decreases at the same film thickness, which leads to the lower scaled normal stress difference at the initial stage of drying. The stress difference shows the distinct



evolution after the maximum. At low  $Pe_L$ , the difference remains at the maximum; however, at high  $Pe_L$ , it decreases. The reasons for this stress development are explained by the evolution of the contact number distribution at the two boundaries. At low  $Pe_L$ , the large–large contact number is higher at the interface, but the large–small contact number is higher at the substrate. These two effects balance each other, resulting in the constant stress difference after the maximum. At high  $Pe_L$ , the large–large and large–small contact numbers are higher at the substrate, leading to a decrease in the stress difference. Interestingly, for all  $Pe_L$ , the scaled normal stress difference increases again at low film thickness ( $H/H_0 < 0.2$ ). At low  $Pe_L$ , a continuing descent of the interface gives rise to the compression of the particle structure, which results in the localization of the stress at the interface. At high  $Pe_L$ , a continuing descent of the interface leads to a sharp increase in the contact between the small particles as well as the arrangement of the small particles, resulting in the localization of the stress at the interface.

In Chapter 4, the force acting on each type of particle is investigated in the drying process of bi-disperse colloidal film. The scaled local force applied to each species is derived by a decomposition of the local normal stress. The local force field is computed for both large and small particles to explain the different behaviors of the two types of particles. At low  $Pe_L$ , the scaled local force is almost 0 inside the film. At high  $Pe_L$ , the scaled local force for the large particle is larger than 1 near the interface, indicating that the large particles outrun the descending interface. However, for the small particle, the scaled local force near the

interface is lower than 1 during the drying process. Therefore, the large particles are depleted from the interface and the small particles are accumulated at the interface, which results in the small-on-top structure. Associating the volume fraction profile with the scaled local force field, we suggest that the strong scaled force for the large particle is attributed to the significant increase of the average number of small particles in contact with the large ones.

This correlation of the particle distribution during drying with the evolution of the normal stress and microstructure is believed to provide insights into the drying process of the mono- and bi-disperse colloidal films. In addition, scaled local force analysis proposed in this study has significance in the examination of the drying mechanism of bi-disperse colloidal films and, further, of the stratification mechanism.

Despite the progress in understanding the formation mechanism of heterogeneous structure in drying of colloidal films, more simulation research is still needed in this area. Specifically, the effect of solvent on the drying mechanism needs thorough investigation with simulations. The short-range HI and capillary force become important as drying proceeds due to the increasing volume fraction of the film, however, existing simulation studies do not take into account both effects. The explicit solvent method that considers convective flow and long-range HI could be further developed to consider short-range HI and capillary force and applied to investigate the formation mechanism of heterogeneous structure.[41, 46]

In addition, simulations could be extended to higher initial volume

fractions of the particles where the short-range HI and capillary force greatly influence the structure formation.[24] Also, they could be extended to higher values of size ratio,[27] and to consider polydisperse colloidal films,[86] sedimentation,[19] and non-spherical colloids.[76] Furthermore, simulations could provide a deeper understanding of the drying mechanism by analyzing the effect of shearing on the structure formation and stress development, the structural heterogeneity in the lateral direction, and the heterogeneous structure observed at the interface due to the capillary force.[41, 47] In this regard, more appropriate study needs to be achieved in the future.

## References

- [1] J. Keddie and A. F. Routh, *Fundamentals of latex film formation: processes and properties*. Springer Science & Business Media, 2010.
- [2] H. Luo, C. M. Cardinal, L. Scriven, and L. F. Francis, "Ceramic nanoparticle/monodisperse latex coatings," *Langmuir*, vol. 24, no. 10, pp. 5552–5561, 2008.
- [3] J. Järnström, P. Ihalainen, K. Backfolk, and J. Peltonen, "Roughness of pigment coatings and its influence on gloss," *Applied Surface Science*, vol. 254, no. 18, pp. 5741–5749, 2008.
- [4] J. Hou, M. Yang, C. Ke, G. Wei, C. Priest, Z. Qiao, G. Wu, and J. Zhang, "Platinum–group–metal catalysts for proton exchange membrane fuel cells: From catalyst design to electrode structure optimization," *EnergyChem*, vol. 2, no. 1, p. 100023, 2020.
- [5] S. Barg, M. D. Innocentini, R. V. Meloni, W. S. Chacon, H. Wang, D. Koch, and G. Grathwohl, "Physical and high–temperature permeation features of double–layered cellular filtering membranes prepared via freeze casting of emulsified powder suspensions," *Journal of Membrane Science*, vol. 383, no. 1–2, pp. 35–43, 2011.
- [6] S. Lim, S. Kim, K. H. Ahn, and S. J. Lee, "Stress development of Li–ion battery anode slurries during the drying process," *Industrial & Engineering Chemistry Research*, vol. 54, no. 23, pp. 6146–6155, 2015.
- [7] M. Stein IV, A. Mistry, and P. P. Mukherjee, "Mechanistic

- understanding of the role of evaporation in electrode processing," *Journal of The Electrochemical Society*, vol. 164, no. 7, p. A1616, 2017.
- [8] A. Nulu, V. Nulu, and K. Y. Sohn, "Silicon and porous MWCNT composite as high capacity anode for lithium-ion batteries," *Korean Journal of Chemical Engineering*, vol. 37, no. 10, pp. 1795–1802, 2020.
- [9] D. D. Brewer, T. Shibuta, L. Francis, S. Kumar, and M. Tsapatsis, "Coating process regimes in particulate film production by forced-convection-assisted drag-out," *Langmuir*, vol. 27, no. 18, pp. 11660–11670, 2011.
- [10] O. D. Velez and S. Gupta, "Materials Fabricated by Micro-and Nanoparticle Assembly—The Challenging Path from Science to Engineering," *Advanced Materials*, vol. 21, no. 19, pp. 1897–1905, 2009.
- [11] J. L. Keddie, "Film formation of latex," *Materials Science and Engineering: R: Reports*, vol. 21, no. 3, pp. 101–170, 1997.
- [12] S. Kim, J. H. Sung, S. Lim, and K. H. Ahn, "A generality in stress development of silica/poly (vinyl alcohol) mixtures during drying process," *Progress in Organic Coatings*, vol. 88, pp. 304–309, 2015.
- [13] J. Lee, S. Sung, Y. Kim, J. D. Park, and K. H. Ahn, "A new paradigm of materials processing—heterogeneity control," *Current Opinion in Chemical Engineering*, vol. 16, pp. 16–22, 2017.
- [14] S. Jaiser, M. Müller, M. Baunach, W. Bauer, P. Scharfer, and W.

- Schabel, "Investigation of film solidification and binder migration during drying of Li-Ion battery anodes," *Journal of Power Sources*, vol. 318, pp. 210–219, 2016.
- [15] I. Nikiforo, J. Adams, A. M. Konig, A. Langhoff, K. Pohl, A. Turshatov, and D. Johannsmann, "Self-stratification during film formation from latex blends driven by differences in collective diffusivity," *Langmuir*, vol. 26, no. 16, pp. 13162–13167, 2010.
- [16] M. P. Howard, A. Nikoubashman, and A. Z. Panagiotopoulos, "Stratification in drying polymer-polymer and colloid-polymer mixtures," *Langmuir*, vol. 33, no. 42, pp. 11390–11398, 2017.
- [17] Y. Ma, H. Davis, and L. Scriven, "Microstructure development in drying latex coatings," *Progress in Organic Coatings*, vol. 52, no. 1, pp. 46–62, 2005.
- [18] R. G. Shimmin, A. J. DiMauro, and P. V. Braun, "Slow Vertical Deposition of Colloidal Crystals: A Langmuir–Blodgett Process?," *Langmuir*, vol. 22, no. 15, pp. 6507–6513, 2006.
- [19] C. M. Cardinal, Y. D. Jung, K. H. Ahn, and L. Francis, "Drying regime maps for particulate coatings," *AIChE Journal*, vol. 56, no. 11, pp. 2769–2780, 2010.
- [20] L. Wang, Y. Wan, Y. Li, Z. Cai, H. L. Li, X. S. Zhao, and Q. Li, "Binary colloidal crystals fabricated with a horizontal deposition method," *Langmuir*, vol. 25, no. 12, pp. 6753–6759, 2009.
- [21] Z. Dai, Y. Li, G. Duan, L. Jia, and W. Cai, "Phase diagram, design of monolayer binary colloidal crystals, and their fabrication based on ethanol-assisted self-assembly at the air/water interface," *ACS*

- Nano*, vol. 6, no. 8, pp. 6706–6716, 2012.
- [22] J. L. Russell, G. H. Noel, J. M. Warren, N.–L. L. Tran, and T. E. Mallouk, "Binary colloidal crystal films grown by vertical evaporation of silica nanoparticle suspensions," *Langmuir*, vol. 33, no. 39, pp. 10366–10373, 2017.
- [23] A. K. Atmuri, S. R. Bhatia, and A. F. Routh, "Autostratification in drying colloidal dispersions: Effect of particle interactions," *Langmuir*, vol. 28, no. 5, pp. 2652–2658, 2012.
- [24] R. Trueman, E. Lago Domingues, S. Emmett, M. Murray, J. Keddie, and A. Routh, "Autostratification in drying colloidal dispersions: experimental investigations," *Langmuir*, vol. 28, no. 7, pp. 3420–3428, 2012.
- [25] A. Utgenannt, R. Maspero, A. Fortini, R. Turner, M. Florescu, C. Jaynes, A. G. Kanaras, O. L. Muskens, R. P. Sear, and J. L. Keddie, "Fast assembly of gold nanoparticles in large–area 2D nanogrids using a one–step, near–infrared radiation–assisted evaporation process," *ACS Nano*, vol. 10, no. 2, pp. 2232–2242, 2016.
- [26] A. Fortini, I. Martin–Fabiani, J. L. De La Haye, P. Y. Dugas, M. Lansalot, F. D'agosto, E. Bourgeat–Lami, J. L. Keddie, and R. P. Sear, "Dynamic stratification in drying films of colloidal mixtures," *Physical Review Letters*, vol. 116, no. 11, p. 118301, 2016.
- [27] D. Makepeace, A. Fortini, A. Markov, P. Locatelli, C. Lindsay, S. Moorhouse, R. Lind, R. P. Sear, and J. L. Keddie, "Stratification in binary colloidal polymer films: Experiment and simulations," *Soft Matter*, vol. 13, no. 39, pp. 6969–6980, 2017.

- [28] L. Brown, C. Zukoski, and L. White, "Consolidation during drying of aggregated suspensions," *AIChE Journal*, vol. 48, no. 3, pp. 492–502, 2002.
- [29] A. F. Routh and W. B. Zimmerman, "Distribution of particles during solvent evaporation from films," *Chemical Engineering Science*, vol. 59, no. 14, pp. 2961–2968, 2004.
- [30] T. Narita, P. Hebraud, and F. Lequeux, "Effects of the rate of evaporation and film thickness on nonuniform drying of film-forming concentrated colloidal suspensions," *The European Physical Journal E*, vol. 17, no. 1, pp. 69–76, 2005.
- [31] R. Trueman, E. L. Domingues, S. Emmett, M. Murray, and A. Routh, "Auto-stratification in drying colloidal dispersions: A diffusive model," *Journal of Colloid and Interface Science*, vol. 377, no. 1, pp. 207–212, 2012.
- [32] M. Schulz and J. Keddie, "A critical and quantitative review of the stratification of particles during the drying of colloidal films," *Soft Matter*, vol. 14, no. 30, pp. 6181–6197, 2018.
- [33] S. H. Im and O. O. Park, "Effect of evaporation temperature on the quality of colloidal crystals at the water–air interface," *Langmuir*, vol. 18, no. 25, pp. 9642–9646, 2002.
- [34] P. Ekanayake, P. McDonald, and J. Keddie, "An experimental test of the scaling prediction for the spatial distribution of water during the drying of colloidal films," *The European Physical Journal Special Topics*, vol. 166, no. 1, pp. 21–27, 2009.
- [35] J. H. Jeong, Y. K. Lee, and K. H. Ahn, "Drying mechanism of



- monodisperse colloidal film: Evolution of normal stress and its correlation with microstructure," *AIChE Journal*, p. e17400, 2021.
- [36] Y. Reyes and Y. Duda, "Modeling of drying in films of colloidal particles," *Langmuir*, vol. 21, no. 15, pp. 7057–7060, 2005.
- [37] S. Cheng and G. S. Grest, "Molecular dynamics simulations of evaporation–induced nanoparticle assembly," *The Journal of Chemical Physics*, vol. 138, no. 6, p. 064701, 2013.
- [38] M. Fujita and Y. Yamaguchi, "Multiscale simulation method for self–organization of nanoparticles in dense suspension," *Journal of Computational Physics*, vol. 223, no. 1, pp. 108–120, 2007.
- [39] B. Chun, T. Yoo, and H. W. Jung, "Temporal evolution of concentration and microstructure of colloidal films during vertical drying: a lattice Boltzmann simulation study," *Soft Matter*, vol. 16, no. 2, pp. 523–533, 2020.
- [40] M. Wang and J. F. Brady, "Microstructures and mechanics in the colloidal film drying process," *Soft Matter*, vol. 13, no. 44, pp. 8156–8170, 2017.
- [41] M. P. Howard, W. F. Reinhart, T. Sanyal, M. S. Shell, A. Nikoubashman, and A. Z. Panagiotopoulos, "Evaporation–induced assembly of colloidal crystals," *The Journal of Chemical Physics*, vol. 149, no. 9, p. 094901, 2018.
- [42] P. Steward, J. Hearn, and M. Wilkinson, "An overview of polymer latex film formation and properties," *Advances in Colloid and Interface Science*, vol. 86, no. 3, pp. 195–267, 2000.
- [43] D. Heyes and J. Melrose, "Brownian dynamics simulations of model

- hard-sphere suspensions," *Journal of non-Newtonian Fluid Mechanics*, vol. 46, no. 1, pp. 1–28, 1993.
- [44] D. R. Foss and J. F. Brady, "Brownian dynamics simulation of hard-sphere colloidal dispersions," *Journal of Rheology*, vol. 44, no. 3, pp. 629–651, 2000.
- [45] M. P. Allen and D. J. Tildesley, *Computer simulation of liquids*. Oxford university press, 2017.
- [46] Y. Tang, G. S. Grest, and S. Cheng, "Stratification of drying particle suspensions: Comparison of implicit and explicit solvent simulations," *The Journal of Chemical Physics*, vol. 150, no. 22, p. 224901, 2019.
- [47] M. Fujita and Y. Yamaguchi, "Development of three-dimensional structure formation simulator of colloidal nanoparticles during drying," *Journal of Chemical Engineering of Japan*, vol. 39, no. 1, pp. 83–89, 2006.
- [48] J. D. Weeks, D. Chandler, and H. C. Andersen, "Role of repulsive forces in determining the equilibrium structure of simple liquids," *The Journal of Chemical Physics*, vol. 54, no. 12, pp. 5237–5247, 1971.
- [49] M. P. Howard, A. Nikoubashman, and A. Z. Panagiotopoulos, "Stratification dynamics in drying colloidal mixtures," *Langmuir*, vol. 33, no. 15, pp. 3685–3693, 2017.
- [50] J. Jover, A. Haslam, A. Galindo, G. Jackson, and E. Müller, "Pseudo hard-sphere potential for use in continuous molecular-dynamics simulation of spherical and chain molecules," *The Journal of*

- Chemical Physics*, vol. 137, no. 14, p. 144505, 2012.
- [51] D. Deb, A. Winkler, M. H. Yamani, M. Oettel, P. Virnau, and K. Binder, "Hard sphere fluids at a soft repulsive wall: A comparative study using Monte Carlo and density functional methods," *The Journal of Chemical Physics*, vol. 134, no. 21, p. 214706, 2011.
- [52] V. Telezki and S. Klumpp, "Simulations of structure formation by confined dipolar active particles," *Soft Matter*, 2020.
- [53] P. Pieranski, "Two-dimensional interfacial colloidal crystals," *Physical Review Letters*, vol. 45, no. 7, p. 569, 1980.
- [54] O. D. Velev, N. D. Denkov, V. N. Paunov, P. A. Kralchevsky, and K. Nagayama, "Direct measurement of lateral capillary forces," *Langmuir*, vol. 9, no. 12, pp. 3702–3709, 1993.
- [55] A. Fortini and R. P. Sear, "Stratification and size segregation of ternary and polydisperse colloidal suspensions during drying," *Langmuir*, vol. 33, no. 19, pp. 4796–4805, 2017.
- [56] B. Todd, D. J. Evans, and P. J. Daivis, "Pressure tensor for inhomogeneous fluids," *Physical Review E*, vol. 52, no. 2, p. 1627, 1995.
- [57] D. Heyes, E. Smith, D. Dini, and T. Zaki, "The equivalence between volume averaging and method of planes definitions of the pressure tensor at a plane," *The Journal of Chemical Physics*, vol. 135, no. 2, p. 024512, 2011.
- [58] H. C. Chu and R. N. Zia, "The non-Newtonian rheology of hydrodynamically interacting colloids via active, nonlinear microrheology," *Journal of Rheology*, vol. 61, no. 3, pp. 551–574,

2017.

- [59] R. N. Zia and J. F. Brady, "Microviscosity, microdiffusivity, and normal stresses in colloidal dispersions," *Journal of Rheology*, vol. 56, no. 5, pp. 1175–1208, 2012.
- [60] Á. Mulero, *Theory and simulation of hard–sphere fluids and related systems*. Springer, 2008.
- [61] P. A. Thompson and M. O. Robbins, "Shear flow near solids: Epitaxial order and flow boundary conditions," *Physical Review A*, vol. 41, no. 12, p. 6830, 1990.
- [62] K. Yeo and M. R. Maxey, "Ordering transition of non–Brownian suspensions in confined steady shear flow," *Physical Review E*, vol. 81, no. 5, p. 051502, 2010.
- [63] S. Inasawa, Y. Oshimi, and H. Kamiya, "Formation kinetics of particulate films in directional drying of a colloidal suspension," *Soft Matter*, vol. 12, no. 32, pp. 6851–6857, 2016.
- [64] P. Schall, D. A. Weitz, and F. Spaepen, "Structural rearrangements that govern flow in colloidal glasses," *Science*, vol. 318, no. 5858, pp. 1895–1899, 2007.
- [65] R. Hartkamp, A. Ghosh, T. Weinhart, and S. Luding, "A study of the anisotropy of stress in a fluid confined in a nanochannel," *The Journal of Chemical Physics*, vol. 137, no. 4, p. 044711, 2012.
- [66] J. Colombo and E. Del Gado, "Stress localization, stiffening, and yielding in a model colloidal gel," *Journal of Rheology*, vol. 58, no. 5, pp. 1089–1116, 2014.
- [67] J. K. Dhont and W. J. Briels, "Rod–like Brownian particles in shear

flow: Sections 3.1–3.9," *Wiley–VCH Verlag GmbH and Co. KGaA*, vol. 2, pp. 147–216, 2007.

- [68] J. F. Brady, "Particle motion driven by solute gradients with application to autonomous motion: continuum and colloidal perspectives," *Journal of Fluid Mechanics*, vol. 667, pp. 216–259, 2011.
- [69] R. P. Sear and P. B. Warren, "Diffusiophoresis in nonadsorbing polymer solutions: The Asakura–Oosawa model and stratification in drying films," *Physical Review E*, vol. 96, no. 6, p. 062602, 2017.
- [70] R. P. Sear, "Stratification of mixtures in evaporating liquid films occurs only for a range of volume fractions of the smaller component," *The Journal of Chemical Physics*, vol. 148, no. 13, p. 134909, 2018.
- [71] J. K. Whitmer and E. Luijten, "Sedimentation of aggregating colloids," *The Journal of Chemical Physics*, vol. 134, no. 3, p. 034510, 2011.
- [72] T. Kaewpetch and J. F. Gilchrist, "Chemical vs. mechanical microstructure evolution in drying colloid and polymer coatings," *Scientific Reports*, vol. 10, no. 1, pp. 1–10, 2020.
- [73] Y. Rahmani, K. Van Der Vaart, B. Van Dam, Z. Hu, V. Chikkadi, and P. Schall, "Dynamic heterogeneity in hard and soft sphere colloidal glasses," *Soft Matter*, vol. 8, no. 15, pp. 4264–4270, 2012.
- [74] G. L. Hunter and E. R. Weeks, "The physics of the colloidal glass transition," *Reports on Progress in Physics*, vol. 75, no. 6, p. 066501, 2012.

- [75] S. Baesch, K. Price, P. Scharfer, L. Francis, and W. Schabel, "Influence of the drying conditions on the particle distribution in particle filled polymer films: Experimental validation of predictive drying regime maps," *Chemical Engineering and Processing—Process Intensification*, vol. 123, pp. 138–147, 2018.
- [76] V. c.–A. Gracia–Medrano–Bravo, J. Groñe, S. Baesch, P. Scharfer, and W. Schabel, "Influence of Particle Shape on the Drying Regime Maps for Platelike Particle–Polymer Composites," *Langmuir*, vol. 36, no. 22, pp. 6245–6253, 2020.
- [77] J. Zhou, Y. Jiang, and M. Doi, "Cross interaction drives stratification in drying film of binary colloidal mixtures," *Physical Review Letters*, vol. 118, no. 10, p. 108002, 2017.
- [78] R. Tatsumi, T. Iwao, O. Koike, Y. Yamaguchi, and Y. Tsuji, "Effects of the evaporation rate on the segregation in drying bimodal colloidal suspensions," *Applied Physics Letters*, vol. 112, no. 5, p. 053702, 2018.
- [79] Y. Tang, G. S. Grest, and S. Cheng, "Stratification in drying films containing bidisperse mixtures of nanoparticles," *Langmuir*, vol. 34, no. 24, pp. 7161–7170, 2018.
- [80] B. He, I. Martin–Fabiani, R. Roth, G. I. Tóth, and A. J. Archer, "Dynamical Density Functional Theory for the Drying and Stratification of Binary Colloidal Dispersions," *Langmuir*, 2021.
- [81] X. Liu, W. Liu, A. J. Carr, D. S. Vazquez, D. Nykypanchuk, P. W. Majewski, A. F. Routh, and S. R. Bhatia, "Stratification during evaporative assembly of multicomponent nanoparticle films,"

*Journal of Chemical Engineering of Japan*, vol. 515, pp. 70–77, 2018.

- [82] Y. Fan and K. Hill, "Theory for shear–induced segregation of dense granular mixtures," *New Journal of Physics*, vol. 13, no. 9, p. 095009, 2011.
- [83] Y. Fan and K. M. Hill, "Phase transitions in shear–induced segregation of granular materials," *Physical Review Letters*, vol. 106, no. 21, p. 218301, 2011.
- [84] L. Staron and J. Phillips, "Stress partition and microstructure in size–segregating granular flows," *Physical Review E*, vol. 92, no. 2, p. 022210, 2015.
- [85] M. Wang and J. F. Brady, "Spectral Ewald acceleration of Stokesian dynamics for polydisperse suspensions," *Journal of Computational Physics*, vol. 306, pp. 443–477, 2016.
- [86] O. Cusola, S. Kivisto, S. Vierros, P. Batys, M. Ago, B. L. Tardy, L. G. Greca, M. B. Roncero, M. Sammalkorpi, and O. J. Rojas, "Particulate coatings via evaporation–induced self–assembly of polydisperse colloidal lignin on solid interfaces," *Langmuir*, vol. 34, no. 20, pp. 5759–5771, 2018.

## 국문 초록

입자계 필름은 크기가 서로 다른 입자, 바인더, 용매 등의 혼합물이기 때문에 건조 과정 중 이들의 분포를 제어하는 것이 매우 중요하다. 잘 분산된 입자계 필름에서도 건조 과정 중 불균일 구조가 형성된다는 것이 알려져 있다. 건조 과정 중 형성되는 불균일 구조에 대해 몇몇 연구들이 진행되었지만, 연구들의 대부분은 불균일 구조가 나타나는 건조 조건을 찾는 데 초점이 맞춰져 있다. 본 학위 논문에서는, 건조 과정 중 응력 및 미세 구조 분석을 통해 불균일 구조가 형성되는 메커니즘을 설명하고자 한다. 복잡한 입자계 필름의 모델 시스템으로서, 단분산 및 이분산 입자계 필름에 대해서 전산 모사 방법론을 사용하여 탐구하였다.

첫째, 단분산 입자계 필름에서는, Brownian dynamics simulation 을 이용해 필름 두께 방향으로의 불균일 구조가 형성되는 과정을 분석하였다. 건조 속도와 입자의 확산 속도의 비가 불균일 구조를 형성하는 주요 인자로 작용하였다. 건조 속도가 확산 속도보다 우세한 조건에서, 하강하는 계면에 입자들이 축적되어 시간이 지날수록 축적 영역의 두께가 증가하였다. 입자의 축적은 수직 응력의 국부화를 유발시켜 계면에서의 수직 응력은 건조 초기부터 증가하였다. 필름 내부에 형성된 수직 응력 기울기가 입자의 알짜 움직임을 유발하는 물리적인 원인을 규명하였다. 또한, 수직 응력 기울기와 미세 구조의 발달 과정을 연관 지음으로써 불균일 구조의 형성 메커니즘을 자세하게 이해할 수 있었다.

둘째, 이분산 입자계 필름에서는, Brownian dynamics simulation 을 이용하여 크기가 작은 입자만으로 이루어진 stratified layer 가 형성되는 과정을 연구하였다. 건조 속도가 입자의 확산 속도보다 우세한 조건에서, 하강하는 계면에 크기가 작은 입자들이 축적되고 stratified layer 를



형성하였다. 계면 부근에 존재하던 크기가 큰 입자들은 기저층 방향으로 밀려나고, stratified layer 아래에 축적 영역을 형성하였다. 계면 아래에 축적된 입자들은 수직 응력의 국부화를 유발하여 계면에서의 수직 응력은 건조 초기부터 증가하였다. 필름 내부에 형성된 수직 응력 기울기가 큰 입자를 계면에서부터 멀어지게 만드는 힘의 물리적인 원인임을 밝혀낼 수 있었다. 또한, 미세 구조 분석과 수직 응력 분석을 연관 지음으로써, 큰 입자와 접촉하는 작은 입자 수의 현저한 증가가 큰 입자를 밀어내는 힘을 유발함을 알아낼 수 있었다.

종합하면, 수직 응력과 미세 구조 발달의 상관관계를 분석함으로써, 건조 과정 중 불균일 구조가 형성되는 메커니즘을 해석할 수 있었다. 본 연구 결과는 건조 과정을 통해 목표로 하는 제품을 형성하는 다양한 기술 분야에서 활용될 수 있을 것으로 기대된다.

**주요어:** 건조, 입자계 필름, 불균일성, 응력, 미세 구조, 입자 확산, 입자 축적, stratification, Brownian dynamics simulation

**학번:** 2016-21054

# Curriculum Vitae

---

Name: Jae Hwan Jeong

Date of Birth: Sep. 5, 1994

Present Address: Bldg.311 #412, School of Chemical and Biological Engineering,  
Seoul National University,

1 Gwanak-ro, Gwanak-gu, Seoul 08826, Korea

Email: scold1@snu.ac.kr

Tel: 82-2-880-1580

---

## Education

- **Master and Ph.D. course**, Seoul National University, Korea  
(03.2016~02.2022)  
School of Chemical and Biological Engineering  
**Advisor:** Prof. Kyung Hyun Ahn
- **BS in Chemical and Biological Engineering**, Seoul National University, Korea  
(02.2016)  
Graduation honors, *Cum Laude*  
School of Chemical and Biological Engineering

## Publications

- **J.H. Jeong**, Y.K. Lee and K.H. Ahn. Stratification mechanism in the bidisperse colloidal film drying process: Evolution and decomposition of normal stress correlated with microstructure. *Langmuir*, 2021
- **J.H. Jeong**, Y.K. Lee and K.H. Ahn. Drying mechanism of monodisperse colloidal film: Evolution of normal stress and its correlation with microstructure. *AIChE J.*, 2021
- W.H. Lee, C.W. Lee, G.D. Cha, B.H. Lee, M.S. Bootharaju, **J.H. Jeong**, S.H. Sunwoo, J.H. Kim, K.H. Ahn, T. Hyeon, D.H. Kim. Floatable photocatalytic platform using elastomer-hydrogel nanocomposites for scalable solar hydrogen production. *Nature*, *in revision*.

## Conferences

- **J. H. Jeong**, Y. K. Lee and K. H. Ahn., Stratification in the drying of bi-disperse colloidal film: Evolution of the normal stress and microstructure, The 14<sup>th</sup> European Coating Symposium (ECS), Brussels, Belgium, 09/2021. (**Oral presentation**) (*online*)
- **J. H. Jeong**, Y. K. Lee and K. H. Ahn., Mechanism of stratification in the drying process of bi-disperse colloidal film, The 20<sup>th</sup> International Society of Coating Science and Technology (ISCST), Minneapolis, MN, USA, 09/2020. (**Oral presentation**) (*online*)
- **J. H. Jeong**, Y. K. Lee and K. H. Ahn., Numerical simulation study of bimodal suspensions during drying process, The 13<sup>th</sup> European Coating Symposium (ECS), Heidelberg, Germany, 09/2019 (**Poster presentation**)

## Research experiences

- **Particle dynamics simulation of colloidal suspension**  
Brownian dynamics (BD) simulation  
Smoothed particle hydrodynamics simulation  
Hydrodynamically coupled Brownian dynamics simulation
- **Finite element method (FEM) simulation**  
Mass transfer (drying model, convection-diffusion equation)  
Resin transfer molding (RTM) process
- **Computational Fluid Dynamics (CFD) software**  
COMSOL Multiphysics  
ANSYS-Fluent

## Other experiences

- **Teaching Assistant:**  
Chemical and Biological Process Lab. (2017.09 - 2017.12)  
Process Fluid Mechanics (2017.03 - 2017.06)  
Physical chemistry (2015.09 - 2016.02)

## **References**

1. Prof. Kyung Hyun Ahn (Ph.D. Advisor)  
School of Chemical and Biological Engineering,  
Seoul National University,  
Gwanak-ro, Gwanak-gu, Seoul 08826, Korea  
**Tel:** +82-2-880-1897  
**Email:** ahnnet@snu.ac.kr
2. Prof. Jae Wook Nam  
School of Chemical and Biological Engineering,  
Seoul National University,  
Gwanak-ro, Gwanak-gu, Seoul 08826, Korea  
**Tel:** +82-2-880-1654  
**Email:** jaewooknam@snu.ac.kr